THERMODYNAMIC EFFICACY OF IRREVERSIBLE MAGNETOCALORIC EFFECT CYCLES

An Undergraduate Research Scholars Thesis

by

TYLER BUFFINGTON

Submitted to the Undergraduate Research Scholars program
Texas A&M University
in partial fulfillment of the requirements for the designation as an

UNDERGRADUATE RESEARCH SCHOLAR

Approved by
Research Advisor: Dr. Patrick Shamberger

May 2016

Major: Mechanical Engineering

TABLE OF CONTENTS

ABSTRACT

Thermodynamic Efficacy of Irreversible Magnetocaloric Effect Cycles

Tyler Buffington
Department of Mechanical Engineering
Texas A&M University

Research Advisor: Dr. Patrick Shamberger
Department of Material Science and Engineering

The discovery of the Giant Magnetocaloric Effect (GMCE) has led to a renewed interest in the prospect of magnetic refrigeration as a more environmentally friendly and efficient alternative to vapor-compression cooling. This effect is observed when certain materials with coupled thermal and magnetic properties undergo a magnetostructural first-order phase transition (FOPT). GMCE materials can exhibit large adiabatic temperature changes (ΔT_{ad}) and isothermal entropy changes (ΔS_m) near 300 K, which provide a basis for refrigeration cycles near room temperature. However, the presence of thermal hysteresis associated with the FOPT has been a major obstacle to the use of GMCE materials for commercial refrigeration. In this paper, a methodology is presented for evaluating the thermodynamic efficacy of GMCE-based Brayton refrigeration cycles. This approach combines a Preisach hysteresis model with the experimentally observed thermal and magnetic properties of a $Ni_{45}Co_5Mn_{36.6}In_{13.4}$ alloy. This methodology predicts that a complete adiabatic FOPT results in a large temperature change in excess of 50 K; however, the full transition requires the application of an unreasonably large magnetic field in excess of 40 T. The model shows that Brayton refrigeration cycles are still possible with the application of a more feasible 5 T magnetic field, but with only a partial FOPT. For these Brayton cycles, we show the effect of varying amounts of rate-independent thermal hysteresis on two

thermodynamic figures of merit: fractional Carnot efficiency and the amount of heat removed from a cold reservoir per cycle. We also present the operational parameters, T_{hot} and T_{cold}, that optimize these figures of merit under different amounts of thermal hysteresis.

.

ACKNOWLEDGMENTS

I would like to thank Dr. Patrick Shamberger for a tremendous research experience the past two years. Working with him has not only helped shape my career interests; it has played a pivotal role in my academic and personal growth.

I would also like to thank Timothy Brown for being an incredible friend and mentor over the course of this project. He guidance and support has helped me succeed in this project and reach my academic goals.

CHAPTER I

INTRODUCTION

Background

Cooling processes are a significant component of the global energy demand, accounting for an estimated 15% of worldwide energy consumption [1]. In the United States, refrigeration processes constitute 25% of the residential electrical power demand and 15% of commercial power demand [2]. It is estimated that magnetic refrigeration can offer a 20-30% efficiency advantage over vapor compression refrigeration processes [3]. In addition, magnetic refrigeration operates without the use of greenhouse gases [4].

Magnetic refrigeration takes advantage of the magnetocaloric effect (MCE) [5]. This effect is most strongly observed in magnetic materials whose thermal and magnetic properties are highly coupled over a specific temperature range [6]. When an MCE material is placed in the presence of a magnetic field, B, it undergoes an entropy change ΔS_m under isothermal conditions, or a temperature change, ΔT_{ad}, under adiabatic conditions [7]. These have been used as figures of merit to quantify a material's suitability as a magnetic refrigerant. In conventional magnetocaloric effect materials, these figures of merit are maximized at the material's curie temperature [5]. Although refrigeration cycles based on MCE were useful for cryogenic cooling, the prospect of commercial magnetic refrigeration was limited in part due to the rarity of MCE materials with sufficiently large ΔS_m and ΔT_{ad} values near 300 K. Gd metal was viewed as an ideal near room temperature refrigerant because of its curie temperature of 293 K and ΔT_{ad} of 14

K; however achieving this temperature change requires the application of a large magnetic field (~7 T), which is commercially unfeasible [8].

The discovery of the Giant Magnetocaloric Effect (GMCE) in $Gd_5(Ge,Si)_4$ in 1997 [9] led to a renewed interest in the prospect of near room temperature magnetic refrigeration. The GMCE describes the extremely large MCE observed in magnetocaloric effect materials as they undergo a first-order phase transition (FOPT) [10]. In GMCE $Gd_5(Si_xGe_{1-x})_4$ alloys, where $0 \leq x \leq 0.5$, it was found that the ΔS_m is 100-400% and the ΔT_{ad} is 25-100% higher than all previous MCE materials [11].

Despite the promising discovery of the GMCE, the thermal hysteresis losses of the FOPT have been shown to be a critical barrier to successful GMCE based refrigeration cycles [12, 13]. The presence of these losses have refined the search for potential magnetic refrigerants. In addition to maximizing ΔS_m and ΔT_{ad}, researchers have sought ways to minimize hysteresis losses in GMCE materials. For example, it has been shown that the introduction of C and H atoms in $NaZn_{13}$-type $La(Fe, Si)_{13}$ compounds is linked with a reduction in hysteresis loss [14].

In addition to the materials-based approaches to improving magnetic refrigeration cycles, some have explored thermodynamic path-based improvements. For example, it has been shown that Ericsson and Brayton cycles with parallel T-S curves during their constant field legs are ideal for conventional MCE refrigeration cycles [15]. Also, it has been shown that active magnetic refrigerator (AMR) cycles offer several advantages [16]. These cycles include regenerative legs in which the MCE material is simultaneously used as the refrigerant and as the regenerator [3].

In addition to efficiency improvements, AMR cycles allow for temperature spans that exceed the ΔT_{ad} of the material [17].

Objectives

The work described in this paper lies at the intersection of material and cycle based improvements to magnetic refrigeration. It is well understood that the presence of hysteresis corresponds to thermodynamic irreversibility [18] and ideally ought to be minimized. Because of this, material scientists are actively searching for methods to reduce hysteresis associated with the FOPT in GMCE materials. However, quantifying the dependence of thermodynamic performance on hysteresis is difficult because of the difficulty of varying the hysteretic response of a material with all other parameters held constant. Furthermore, investigating a wide range of cycles is impractical through experimentation. By combining the experimentally determined magnetothermal properties of a $Ni_{45}Co_5Mn_{36.6}In_{13.4}$ alloy with a Preisach based hysteresis model, this paper predicts the effect of varying hysteresis amounts on the thermodynamic performance of GMCE based Brayton cycles. Furthermore, this paper seeks to determine the set of hot and cold reservoir temperatures (T_H and T_C) that optimizes the thermodynamic performance of the Brayton cycles. In this paper, thermodynamic performance refers to two figures of merit: the fractional Carnot coefficient of performance (η) and the amount of heat removed from the cold reservoir (Q_C). By meeting these objectives, this paper seeks to help researchers quantitatively understand how a given change in a material's hysteresis affects its utility as a Brayton cycle refrigerant. Furthermore, understanding the optimal operating conditions (T_H and T_C) to run GMCE based Brayton cycles is vital for system design.

Adaptation of conventional thermodynamic cycles to magnetic systems

This project involves an examination of GMCE based Brayton cycles. Since these cycles are typically designated for gases, it is necessary to establish analogous thermodynamic properties for magnetocaloric systems. Internal magnetic field is established to be analogous to pressure and magnetization is analogous to volume. In conventional gas cycles, Brayton, Carnot, and Ericsson cycles consist of isothermal, adiabatic, and isobaric processes. These correspond to isothermal, adiabatic, and iso-field processes in magnetic systems, respectively. Isochoric processes are analogous to constant magnetization processes; however, controlling the magnetization in the material is difficult, so these processes are generally impractical. A summary of relevant MCE cycles is shown in Table 1.

Table 1: A summary of the relevant MCE refrigeration cycles

Cycle Type	ΔB (Field)	Heating/Cooling
Carnot	Adiabatic	Isothermal
Ericsson	Isothermal	Iso-field[1]
Brayton	Adiabatic	Iso-field
Stirling	Isothermal	Iso-magnetic
Otto	Adiabatic	Iso-magnetic

[1] Note, the Ericcson cycle is regenerative. Heating and cooling also occur along the isothermal ΔB.

CHAPTER II

METHODS

Simulation framework and rationale

Hysteresis refers to the path dependent branching of a system's output based on its history of inputs [19]. Specifically, this paper explores thermal hysteresis associated with the FOPT in a $Ni_{45}Co_5Mn_{36.6}In_{13.4}$ alloy. In this alloy, the FOPT occurs between a low entropy/temperature phase, α and a high entropy/temperature phase, β. The $\alpha \rightarrow \beta$ transition can be induced by a sufficient increase in temperature or magnetic field and the $\beta \rightarrow \alpha$ transition can be induced by a sufficient overall reduction of these parameters. An increase in magnetic field drives the $\alpha \rightarrow \beta$ FOPT which leads to a temperature *decrease* under adiabatic conditions or an entropy *increase* under isothermal conditions. Therefore, $Ni_{45}Co_5Mn_{36.6}In_{13.4}$ alloy is referred to as an *inverse magnetocaloric effect* material because conventional MCE materials exhibit adiabatic temperature increases or isothermal entropy reductions [20]. The thermal hysteresis explored in this paper manifests as a separation between the $\alpha \rightarrow \beta$ and $\beta \rightarrow \alpha$ phase transitions.

A primary objective of this paper is to understand how different amounts of thermal hysteresis affect the thermodynamic performance of the refrigerant. Varying the hysteresis width, ΔT_{hyst}, while keeping all other material parameters fixed is very difficult to achieve experimentally [7]. However, this experiment can be reasonably simulated using a computational model. Though it is held constant at 2 K in the results reported in this paper, the model also allows for varying the elastic width, ΔT_{elast}. This parameter describes the width of the range of equivalent driving force temperatures (θ). Both ΔT_{Hyst} andΔT_{Elast} are illustrated in Figure 1.

All modeling was done using MATLAB R2014a. The model implemented experimentally observed thermal and magnetic properties of both the α and β phases of a $Ni_{45}Co_5Mn_{36.6}In_{13.4}$ alloy. A Debye temperature model was used to fit entropy values for both phases over the span of 0 to 500 K and from 0 to 7 T. A Brillouin model was also used to fit magnetization values over the same range of temperatures and magnetic fields. The curie temperatures of the α and β phases were set to 70 and 388 K respectively, and the Debye temperatures were set to 426 and 340 K respectively. The saturated magnetizations were 12 and 155 Am^2/kg for the α and β phases respectively, and the spin moment indices were 18.5 and 2.5 respectively. The Sommerfield constants were set to zero for both phases.

Assumptions

Equivalence of temperature and magnetic field as driving forces

The key assumption of the model is that temperature and magnetic fields are treated as equivalent driving forces for phase changes. This arises from the experimental observation that the fundamental driving force for a FOPT is a difference in the Gibbs free energy of the α and β phases. The Gibbs free energy for a magnetic material is defined in equation (1)

$$G = U - BM - TS \tag{1}$$

where U is the internal energy of the material, B is the magnetic field, M is the magnetism, T is the temperature and S is the entropy. Expressing equation (1) in differential form gives

$$dG = dU - MdB - BdM - TdS - SdT \tag{2}$$

From the first law of thermodynamics for a magnetic system,

$$dU = TdS + BdM \tag{3}$$

Substituting equation (3) into (2) yields equation (4).

$$dG = -MdB - SdT \tag{4}$$

Because the driving force for the FOPT is the difference in Gibbs free energy between the α and β phases, constant driving force contours are calculated using the condition that $dG^{\alpha} = dG^{\beta}$. This yields the magnetic Clausius-Clapeyron equation (5), which describes the slope of a constant driving force contour in T-B space.

$$\left.\frac{dB}{dT}\right|_{\Delta G} = -\frac{S^{\beta} - S^{\alpha}}{M^{\beta} - M^{\alpha}} \tag{5}$$

These contours allow for the expression of the driving force from any temperature-field pair as an equivalent driving force at zero field. This equivalent driving force temperature at zero field (θ) is simply the intercept of point's contour with the temperature axis. An illustration of this concept is shown in Figure 1.

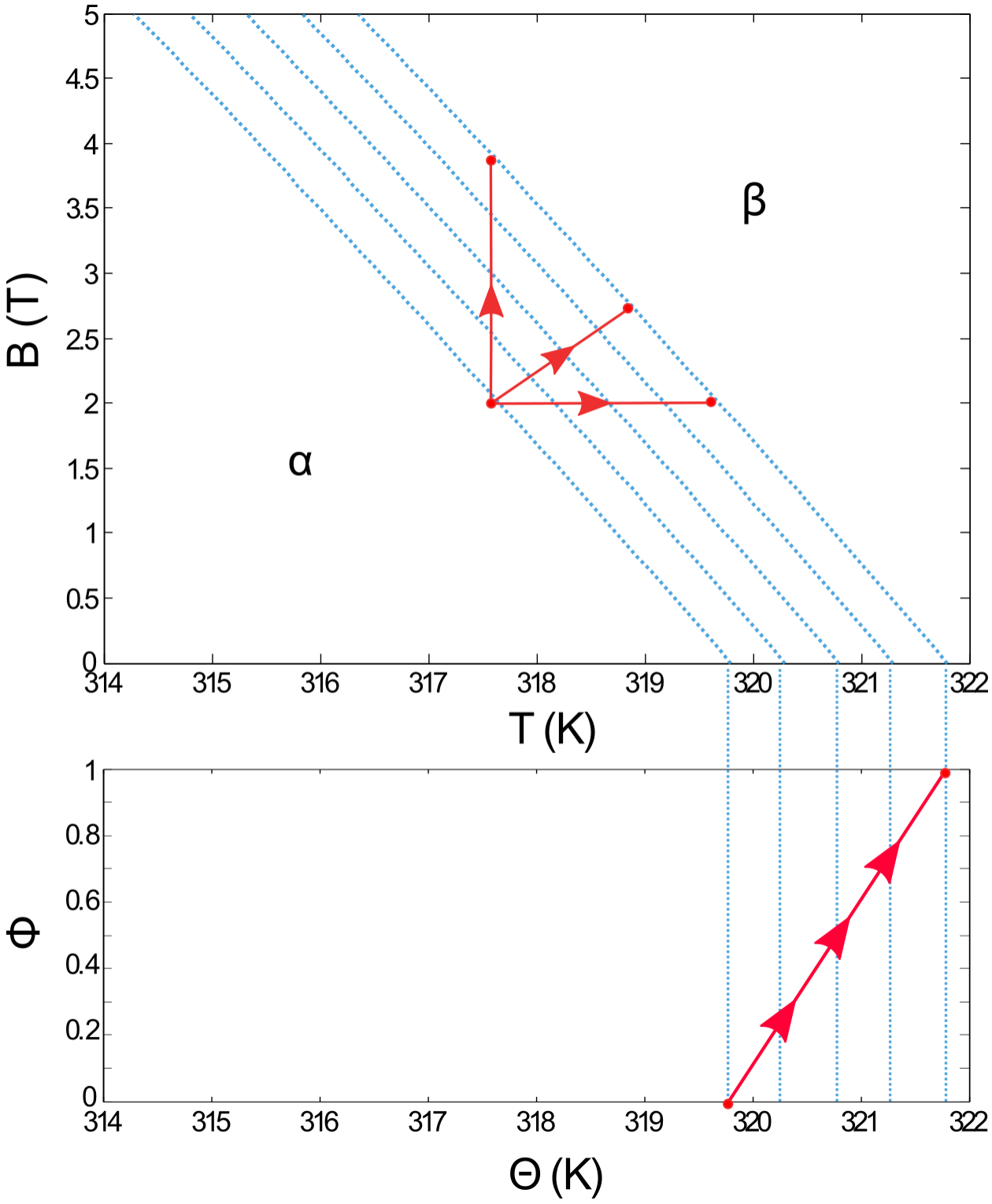

Figure 1: An illustration of the constant driving force assumption.

Along the blue lines, calculated from equation (5), ΔG is constant. For any point in T-B space, a constant driving force contour can be drawn from the point to the temperature axis. The intercept with the temperature axis (θ) represents a condition in which ΔG will be the same, but at zero field. Although the fraction of the β phase (ϕ) during the $\alpha \rightarrow \beta$ transition is a function of both temperature and field, from this assumption, it can be said to be a function of only θ. Figure 1 also shows three different paths that induce the $\alpha \rightarrow \beta$ FOPT, but they all are equivalent paths in the ϕ vs θ plot.

The main advantage of this assumption is that it allows the hysteresis width to be generalized in terms of a driving force separation between the forward and reverse phase transitions. . The hysteretic response of the material is equivalent in terms of Gibbs free energy for temperature and field induced transformations. Previous experimental work validates this assumption [21]. Based on this, hysteresis is modeled as the width between the $\alpha \rightarrow \beta$ and $\beta \rightarrow \alpha$ transformation lines in a ϕ vs θ plot. This illustration is shown in Figure 2.

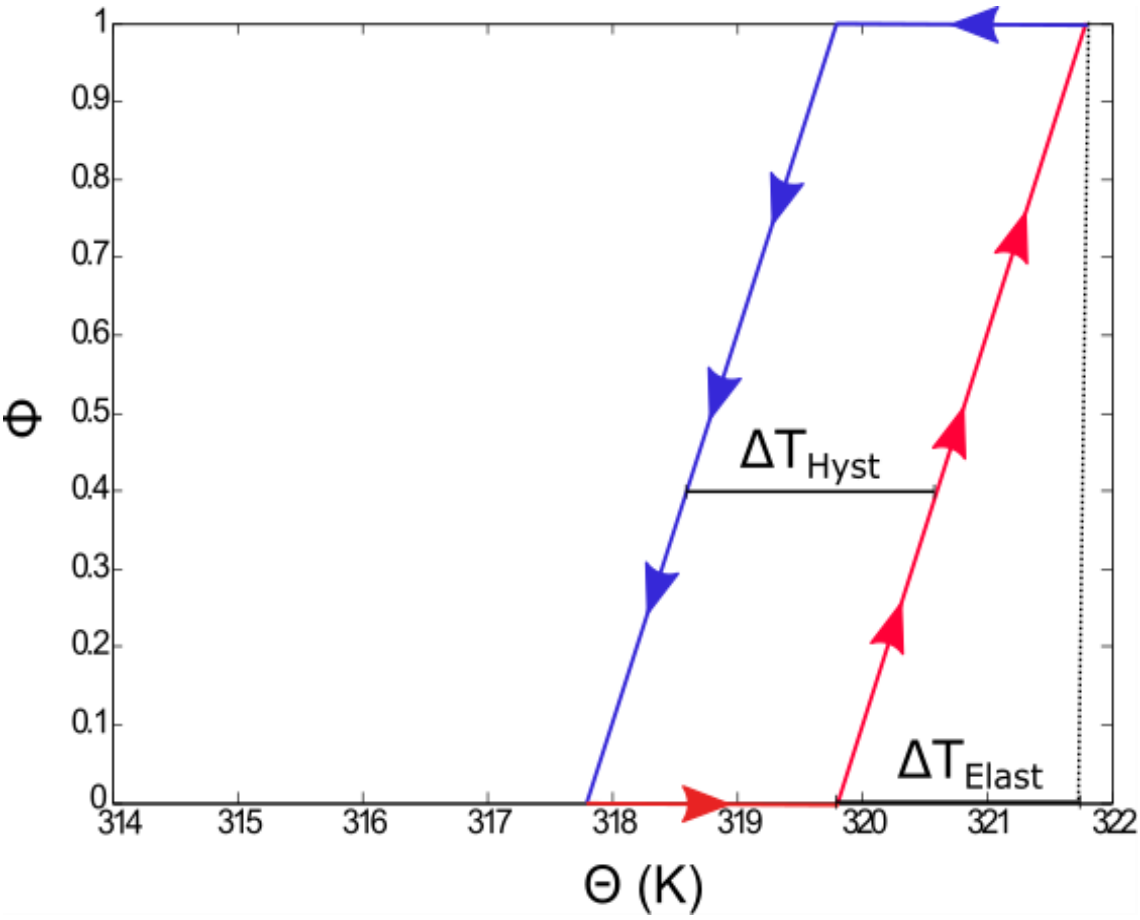

Figure 2: An illustration of how hysteresis is modeled.

The red line shows the $\alpha \rightarrow \beta$ transformation as the driving force is increased. Once the FOPT is complete, the driving force is lowered along the blue line. However, due to the presence of hysteresis, it occurs over a different range of θ values than the $\alpha \rightarrow \beta$ transition. The width between the lines is defined as the hysteresis width, ΔT_{Hyst}. Also, the phase fraction is assumed to change linearly with θ for both the $\alpha \rightarrow \beta$ and $\beta \rightarrow \alpha$ phase transitions. The size of the interval of θ values over which each linear transformation occurs is defined as the elastic width (ΔT_{Elast}). It is fixed at 2 K for all results reported in this paper.

Thermodynamic irreversibility

This paper only considers the thermodynamic irreversibility associated with the thermal hysteresis of the FOPT. In reality, there is thermodynamic irreversibility due to magnetic hysteresis and temperature gradients within the system. These irreversibilites are not considered in this paper because they are generally much smaller than those due to FOPT hysteresis Furthermore, this paper assumes that the $\alpha \rightarrow \beta$ FOPT is reversible and all thermodynamic irreversibility is assumed to arise from the $\beta \rightarrow \alpha$ FOPT. Although in reality, both transitions would likely exhibit irreversibility from hysteresis, this assumption has a minimal effect on the results outlined in this paper because all figures of merit are based on analysis of the full cycle. An analysis of a full cycle will capture the total irreversibility of both transitions, so the distribution of the total irreversibility between the transitions does not affect the determination of the cycle's performance.

Thermodynamic analysis

Refrigeration cycles involve transferring heat from a low temperature reservoir to a high temperature reservoir. By the second law of thermodynamics, this process requires a work input to the system. By the first law of thermodynamics,

$$\delta Q - \delta W = dU \tag{6}$$

where Q and W represent heat and work transfer across the system boundary, and U is the internal energy of the refrigerant. In magnetic refrigeration cycles, the only work transfer is magnetic work, shown in equation (7).

$$\delta W = -BdM \tag{7}$$

The entropy balance for closed systems is shown in equation (8).

$$dS = \frac{\delta Q}{T_B} + dS_{irr} \tag{8}$$

where dS is the differential change in system entropy, T is the boundary temperature of the system, and S_{irr} is the irreversible entropy generation during a process. It should be noted that in conventional irreversible thermodynamics, the entropy generation is due to spatial property gradients within the system [18]. This usually leads to an analysis with the system defined such that its boundary is at ambient conditions. This ensures a uniform boundary temperature where $T_B = T_0$, where T_0 is the ambient temperature [22]. This is done because a non-uniform boundary temperature introduces great mathematical difficulty in using equation (8) to quantify energy flows. However, in this paper, the entropy generation is due to the inherent irreversibility of thermal hysteresis rather than spatial gradients. Multiplying both sides of equation (8) by T and solving for δQ gives equation (9).

$$\delta Q = TdS - TdS_{irr} \tag{9}$$

Then, substituting equations (7) and (9) into equation (6) gives equation (10).

$$TdS - TdS_{irr} + BdM = dU \tag{10}$$

Integrating around a cycle gives equation (11).

$$\oint TdS - \oint TdS_{irr} + \oint BdM = \oint dU \tag{11}$$

Because U is a state variable, for any complete cycle, $\oint dU = 0$. Thus equation (11) simplifies to

$$\oint BdM = -\oint TdS + \oint TdS_{irr} \tag{12}$$

Each term in equation (12) holds a physical meaning. $\oint BdM$ represents the net work input into the refrigeration system. $-\oint TdS$ represents the net available refrigeration work done to transfer heat from the cold reservoir to the hot reservoir [7]. $\oint TdS_{irr}$ represents the irreversible energy dissipation during a refrigeration cycle. Thus, equation (12) can be stated as

$$W_{in} = W_{ref} + I \tag{13}$$

Equation (13) is useful for understanding the energy flows in the system. In order for a refrigerator to transfer heat from a cold reservoir to a hot reservoir, it requires a work input, W_{in}. Some of this work is used as refrigeration work (W_{ref}) and some is "lost" as the result of thermodynamic irreversibility. These energy flows are shown in Figure 3.

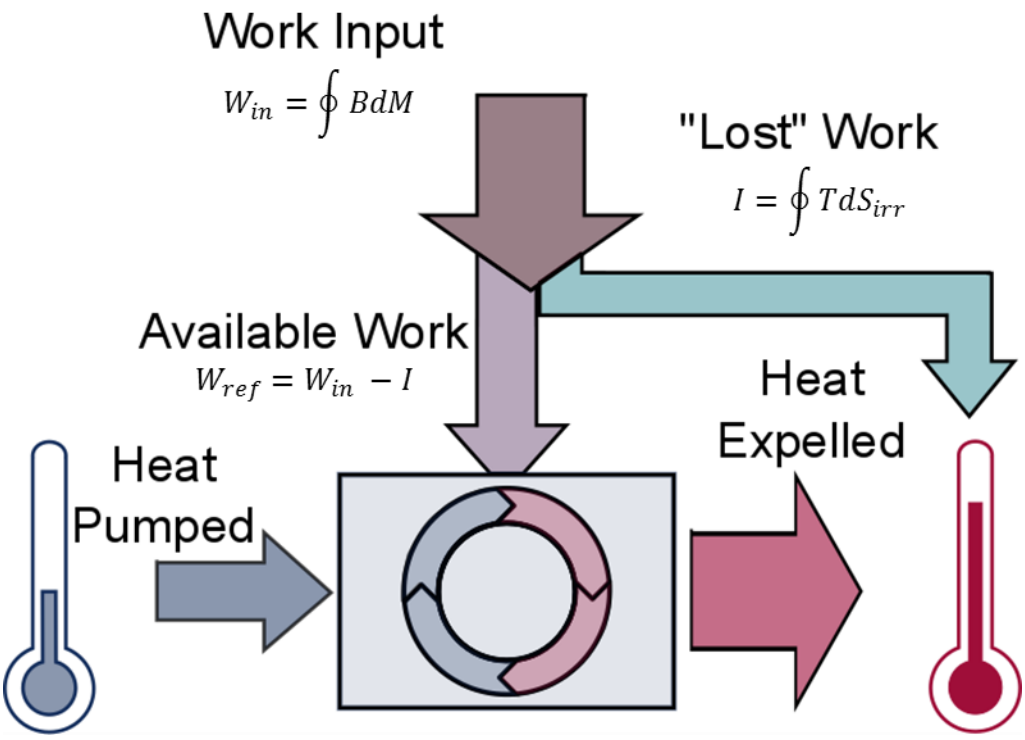

Figure 3: An illustration of the energy flows of the refrigeration system [23]. Image used with permission.

Given the driving force equivalence of temperature and magnetic field and the assumption that all irreversibility is due to hysteresis, I depends only on the hysteresis width for any cycle that involves a full $\alpha \rightarrow \beta$ and $\beta \rightarrow \alpha$ transition.

Modeling adiabatic paths

Method

The simulation of irreversible Brayton cycles required modeling both reversible and irreversible adiabatic field changes. Given the previously stated assumptions, all thermodynamic irreversibility is expected to occur along the $\beta \rightarrow \alpha$ transition, and all other paths are assumed to be reversible. Any path that is both adiabatic and reversible is isentropic based on equation (8). Therefore, any path that is either in a single-phase region or along the $\alpha \rightarrow \beta$ can be modeled

simply finding a set a points with the same entropy. So, for any two points A and B that lie on an adiabatic reversible path, it can be said that

$$S_A = S_B \tag{14}$$

If point A is known, the model can iterate to the correct point B that satisfies equation (14) using the secant method (see Secant method).

Along the $\beta \rightarrow \alpha$ path, entropy must increase because it is irreversible. In order to quantify this entropy increase, a cycle consisting of three paths is considered. Figure 4 shows an illustration of this cycle in T-B space.

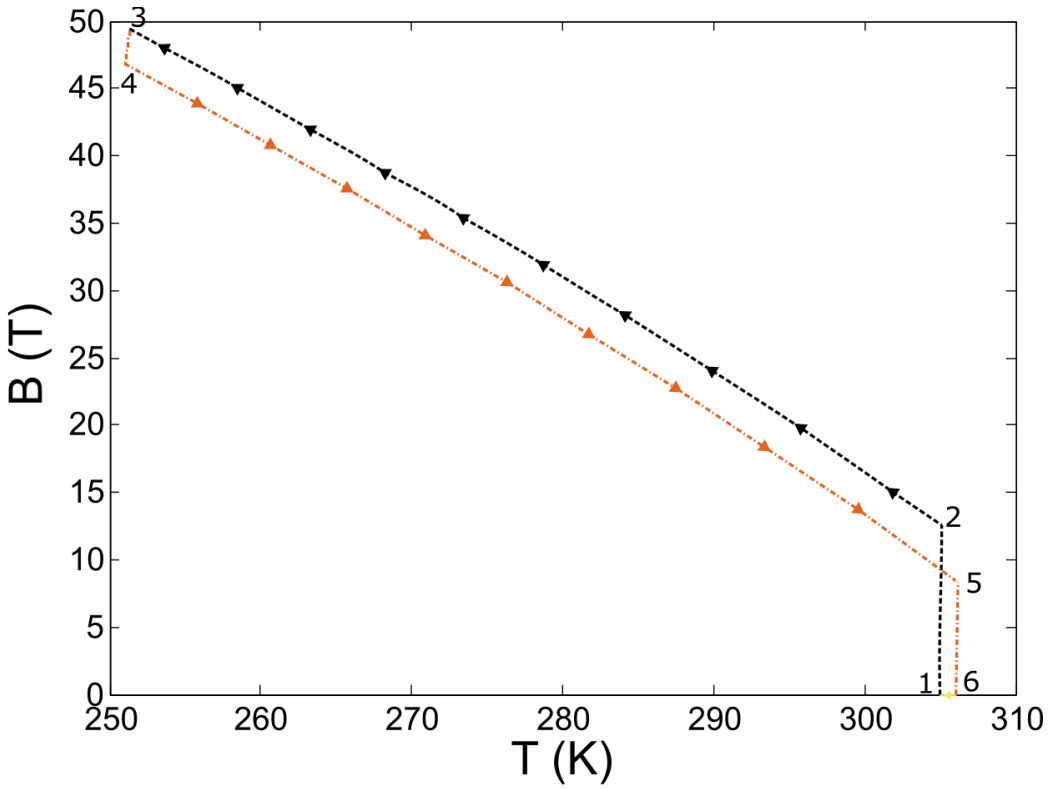

Figure 4: The cycle used to determine the entropy generation along an irreversible adiabatic path with $\Delta T_{Hyst} = 2K$ and $\Delta T_{Elast} = 2K$.

The first path is an adiabatic magnetization during which the full $\alpha \rightarrow \beta$ transition is induced with a magnetic field (black line). Then the field is reduced to zero, returning the material to the α phase (orange line). By the Clausius inequality for irreversible cycles ($\oint \frac{\delta Q}{T} < 0$), a final zero field reversible heat rejection leg is required to complete the cycle (yellow line). The material begins in the α phase at zero field at point 1. From point 1 to 2, the field increased in the pure α phase. Point 2 represents the beginning of the $\alpha \rightarrow \beta$ phase transition which completes at point 3. The field is then lowered, but because of hysteresis, the material remains in the pure β phase from point 3 to point 4. The irreversible $\beta \rightarrow \alpha$ transition occurs between points 4 and 5. The field is further lowered from point 5 to point 6 as the material is in the pure α phase. Because of

the entropy generation that occurs between points 4 and 5, point 6 is at a higher temperature than point 1. To complete the cycle, a reversible heat rejection leg is required from point 6 to point 1.

Since the demagnetization from point 4 to point 5 is the only irreversible process in this cycle, it follows that

$$\int_4^5 TdS = I\left(\Delta T_{Hyst}\right) = \int_4^5 TdS_{irr} \tag{15}$$

Because ϕ decreases linearly with a decreasing driving force, the energy dissipated along the irreversible transition also linearly increases with decreasing ϕ. For a given phase fraction decrease ($\Delta\phi$) between two points along the $\beta \rightarrow \alpha$ transition A and B,

$$\int_A^B TdS = \Delta\phi I\left(\Delta T_{Hyst}\right) = \int_A^B TdS_{irr} \tag{16}$$

Equation (16) describes how points along the irreversible phase transition are defined for a given phase fraction step ($\Delta\phi$). The size of $\Delta\phi$ depends on the user specified resolution of the path. I is calculated based on the hysteresis width, ΔT_{Hyst}. Point A represents a point along the path that is defined, and using the secant method, the model iterates to a point B that satisfies equation (16). The right side of this equation is evaluated using the built in trapezoidal integration function in MATLAB.

Validation

To ensure the internal consistency of the irreversible adiabatic path methodology, a test has been conducted on the cycle shown in Figure 4 based on the path independence of state variables

Internal energy is a state variable, around any complete cycle it must follow that

$$\oint dU = 0 \tag{17}$$

From equations (6) through (8), for any two thermodynamic states A and B, whose path consists only of magnetic work and reversible heat transfer ($\delta W_{in} = BdM$ and $\delta Q_{rev} = TdS$)

$$\int_A^B dU = \int_A^B BdM + \int_A^B TdS \tag{18}$$

In Figure 4, the path from points 1 to 6 are adiabatic, and therefore consists only of magnetic work ($\delta Q = 0$),

$$\int_1^6 dU = \int_1^6 BdM \tag{19}$$

The path from 6 to 1 is done at zero field, so the magnetic work is zero. Therefore, this path consists only of reversible heat transfer,

$$\int_6^1 dU = \int_6^1 TdS \tag{20}$$

Combining equations (17) through (20), it must follow that

$$\int_1^6 BdM + \int_6^1 TdS = 0 \tag{21}$$

This means that the magnetic work input along the adiabatic legs must equal the heat output along the zero field leg to return the material to its initial internal energy. Furthermore, based on equations (12) and (13), it must follow for any cycle that

$$\oint BdM = -\oint TdS + I \tag{22}$$

Using MATLAB's trapezoidal integration function, the cycle in Figure 4 is consistent with equation (21) and (22) within .1 Joules, indicating that the adiabatic path methodology is consistent with the rest of the modeling framework.

The secant method

Description

The secant method is used to iterate to desired points along adiabatic paths. It makes an initial guess of the next point along a given adiabatic path. In both the reversible case and the irreversible case, the left side of the equation is defined (equations (14) and (16)). The right side depends on the "guessed" point B. The error associated with the guess can then be calculated by

evaluating the difference between the left and right side of the equation. Then, another point is selected with a slightly lower magnetic field than the original guess. This allows the model to quantify how much the right side of the equation changes with respect to a change in the magnetic field. It then can generate a new guess at a new magnetic field based on the error of the first guess and the slope of the right side of the equation with respect to magnetic field.

Example

An isentropic leg during a constant phase fraction is computed with an iterative secant method to evaluate points at which both the entropy, S, and the phase fraction, ϕ. Input arguments are the initial field and temperature (B_{low} and T_{low}), and the final field, B_{high}. The entropy is evaluated at B_{low} and T_{low}. All subsequent data points are generated so that their entropy remains equal to this initial entropy. In other words,

$$S_0 = S_1 = S_n \tag{23}$$

The solver then determines a new magnetic field, B_1 based on the specified resolution and the magnetic field range, $B_{high} - B_{low}$ shown below,

$$\Delta B = \frac{B_{high} - B_{low}}{B_{res}} \tag{24}$$

$$B_1 = B_{low} + \Delta B \tag{25}$$

Where ΔB is the field step, and B_{res} is the field resolution. Then the solver generates a new entropy,

$$S_1 = S(T_{low}, B_1) \tag{26}$$

This increase in field reduces the overall entropy, which requires a compensating temperature increase. The solver calculates the error,

$$Error = S_0 - S_1 \tag{27}$$

The solver then estimates the derivative of the entropy with respect to temperature at a constant field, B_1. This is done by evaluating a secant line over a small temperature span, ΔT,

$$\left(\frac{\partial S}{\partial T}\right)_B \approx \frac{S_1 - S(T_{low} - \Delta T, B_1)}{\Delta T} \tag{28}$$

Then the new temperature T_1 is estimated through the following adaption of the secant method,

$$T_1 = T_{low} - \frac{error}{\left(\frac{\partial S}{\partial T}\right)_B} \tag{29}$$

The solver then repeats the process replacing T_{low} with T_1 until error is below a specified convergence tolerance.

CHAPTER III

RESULTS

Adiabatic paths at different hysteresis widths

Cycle similar to the one shown in Figure 4 were generated for several different hysteresis widths. The results are shown in Figure 5.

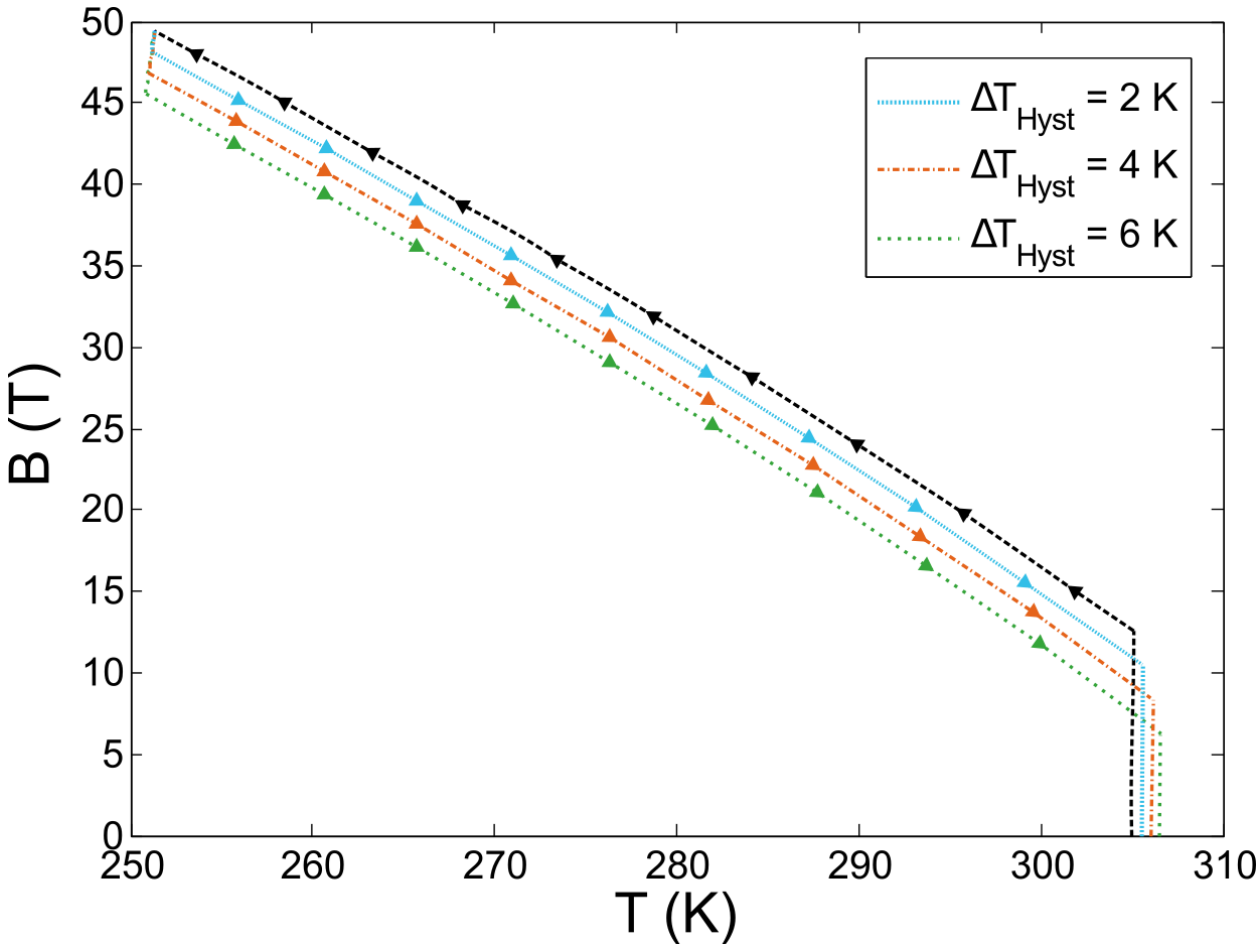

Figure 5: Adiabatic magnetization and demagnetizations between $\phi = 0$ and $\phi = 1$ at different hysteresis widths

Because the $\alpha \rightarrow \beta$ transition is reversible, the refrigerant follows the black line for all three hysteresis widths. The path along the black line ends when $\phi = 1$. Note that a magnetic field in

excess of 45 T is required to complete the phase transition through an adiabatic magnetization. Because of different amounts of hysteresis, different paths are taken during the demagnetization. As the hysteresis width is increased, the temperature at the end of the demagnetization is increased. As a result, a heat rejection leg (not shown) at zero field would be required to complete each cycle. This is consistent with the Clausius inequality for irreversible cycles ($\oint \frac{\delta Q}{T} < 0$). Furthermore, as the hysteresis width (ΔT_{Hyst}) increases, more work is required to complete the $\alpha \rightarrow \beta$ and $\beta \rightarrow \alpha$ transitions, which requires more heat rejection to complete a cycle (equation (21)).

Brayton cycle example

Combining adiabatic field changes with iso-field heating/cooling legs produces Brayton refrigeration cycles (Table 1). An example of a Brayton cycle in T-B space from 0-5 T is shown in Figure 6. Because of the extremely large magnetic fields (> 45 T) required to complete a full $\alpha \rightarrow \beta$ transition, Brayton cycles at more reasonable fields involve only partial phase transformation.

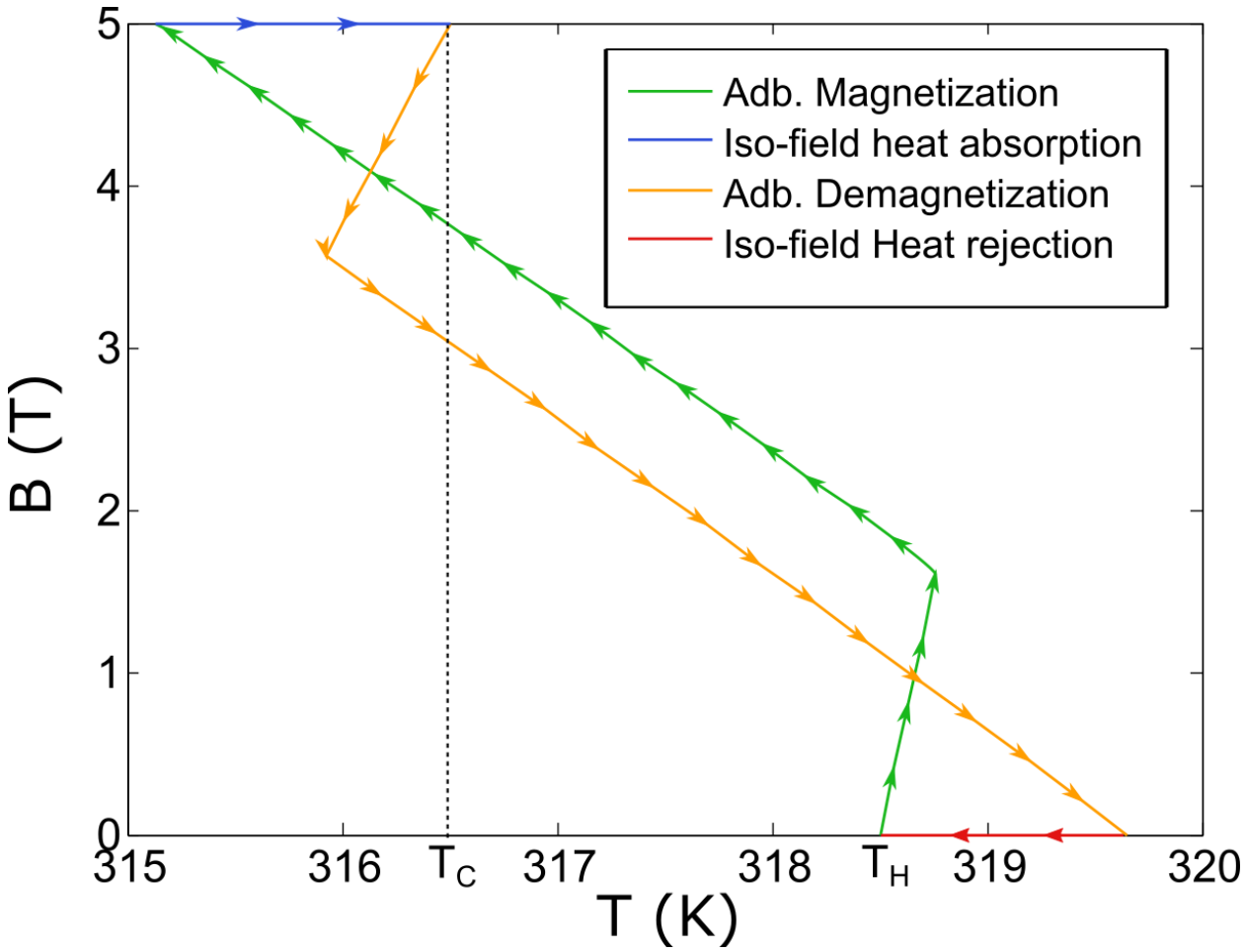

Figure 6: An example of a Brayton cycle in T-B space with $\Delta T_{Hyst} = 2K$

An adiabatic magnetization occurs along the green line at a constant phase fraction of $\phi = .35$. When the refrigerant reaches the phase boundary, a partial phase transformation occurs from $\phi = .35$ to $\phi = .4029$. The magnetization process ends at 5 T because of an assumed practical magnetic field limit. The temperature of the material is now below T_C and can absorb heat from the cold reservoir at a constant 5 T field until $T = T_C$. This process occurs along the blue line. Once the heat absorption from the cold reservoir is complete, the material is demagnetized along the orange line. The material remains in the pure β phase as the field is reduced until it reaches the phase boundary. A partial $\beta \rightarrow \alpha$ transformation then occurs and continues until the material

is at zero field. The material is then above the temperature of the hot reservoir (T_H) and can reject heat until $T = T_H$ along the red line, completing the cycle. The net result of this cycle is that the refrigerant absorbed heat from a cold reservoir and rejected it to a hot reservoir, thereby satisfying the requirements of a refrigerator.

Figure 7 shows the same Brayton cycle in ϕ-θ space. Note, that the cycle does not involve a full transition between the α and β phases.

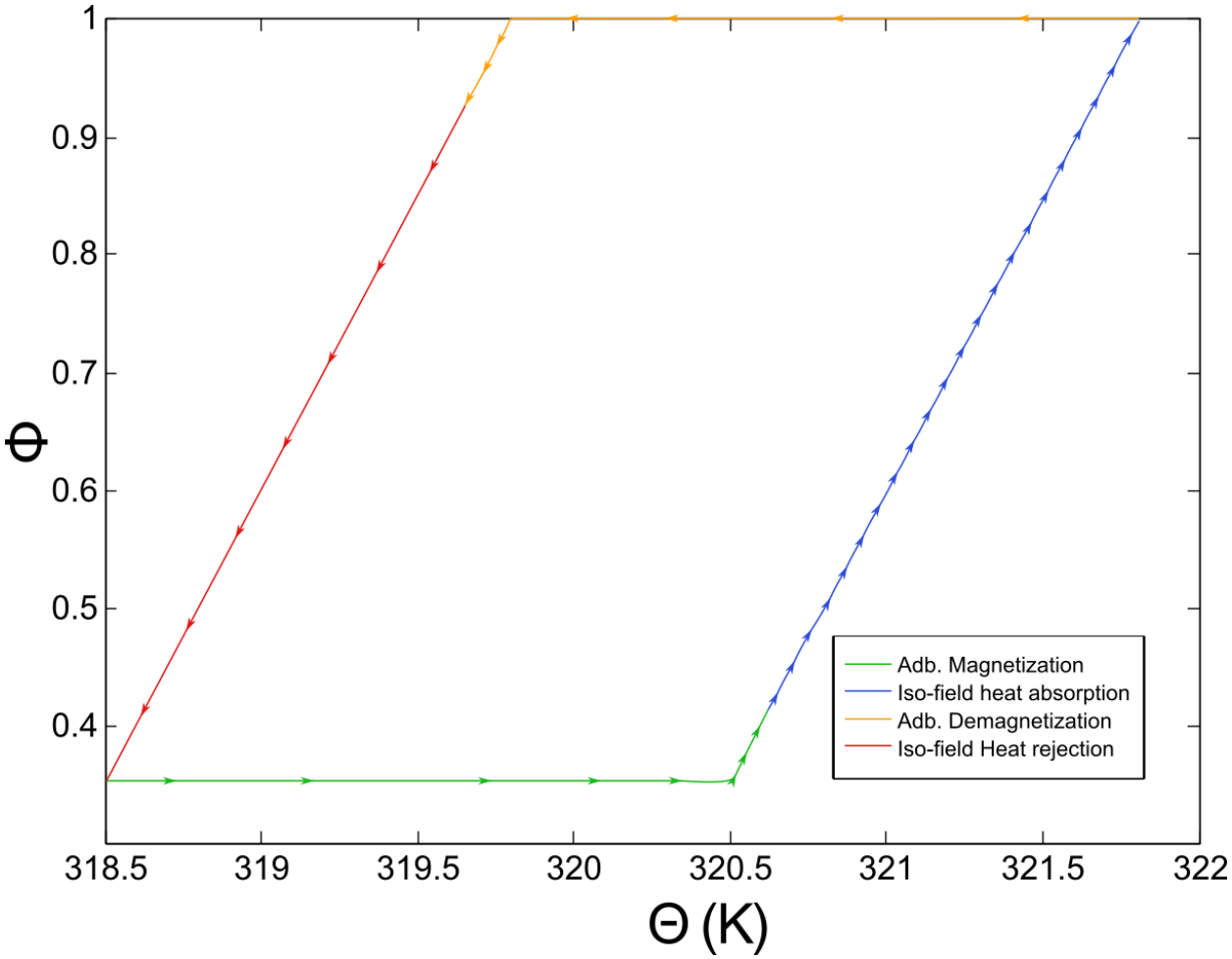

Figure 7: The phase fraction evolution during each leg of the example Brayton cycle.

This same cycle is shown in S-T space in Figure 8.

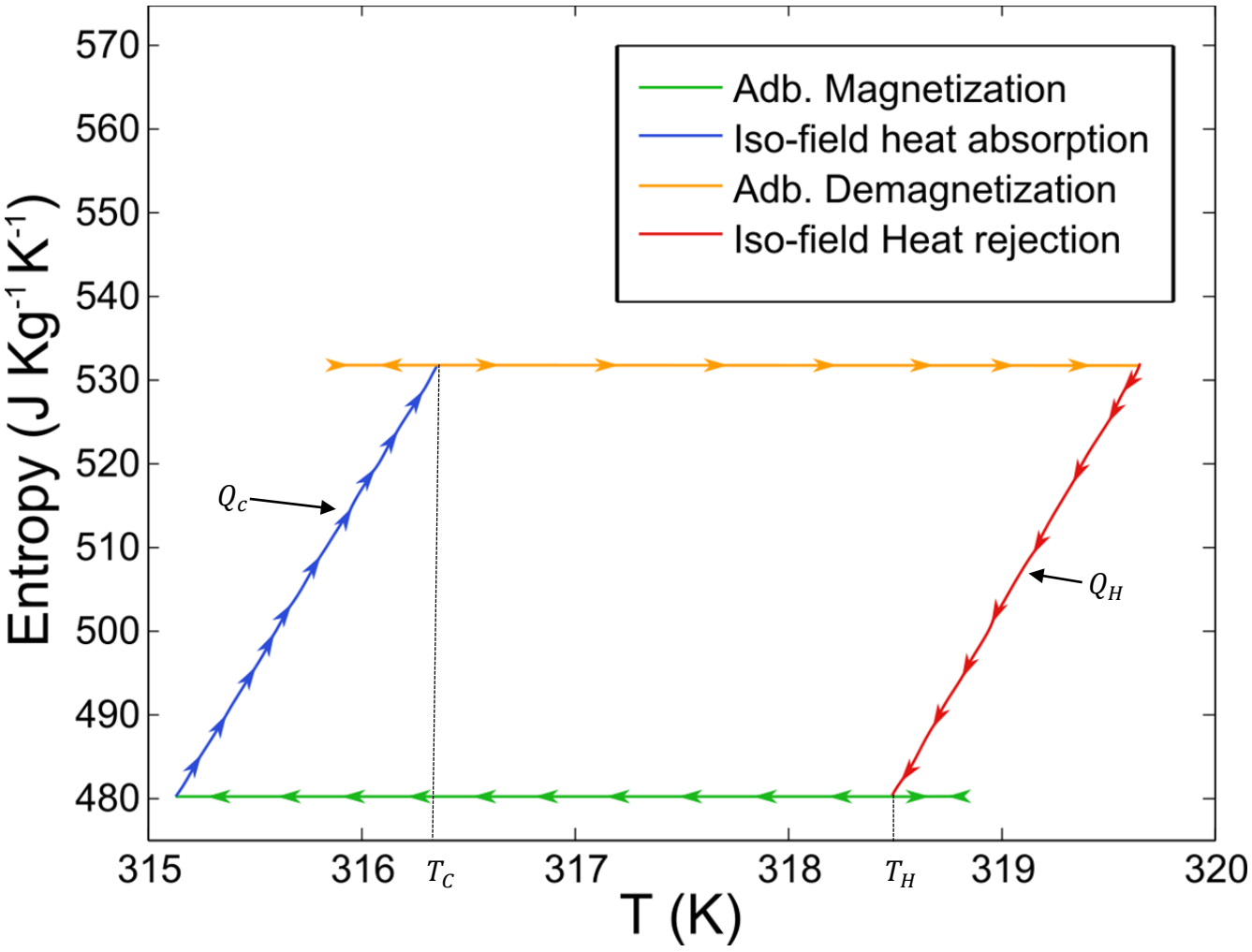

Figure 8: An entropy vs. temperature diagram for the same Brayton cycle shown in Figure 6.

The red and blue lines shown iso-field contours in Figure 8. The green line shows the magnetization process. Since this process is reversible and adiabatic, it is isentropic. The orange line includes the adiabatic demagnetization, which is irreversible. Although the orange line appears isentropic, there is a small entropy increase along this path. However, it is difficult to see because the amount of phase transformation is quite small. This concept is shown in equation

(16), in which a small $\Delta\phi$ leads to a small energy dissipation, and therefore small entropy generation. Finally, this cycle is shown in B-M space in Figure 9.

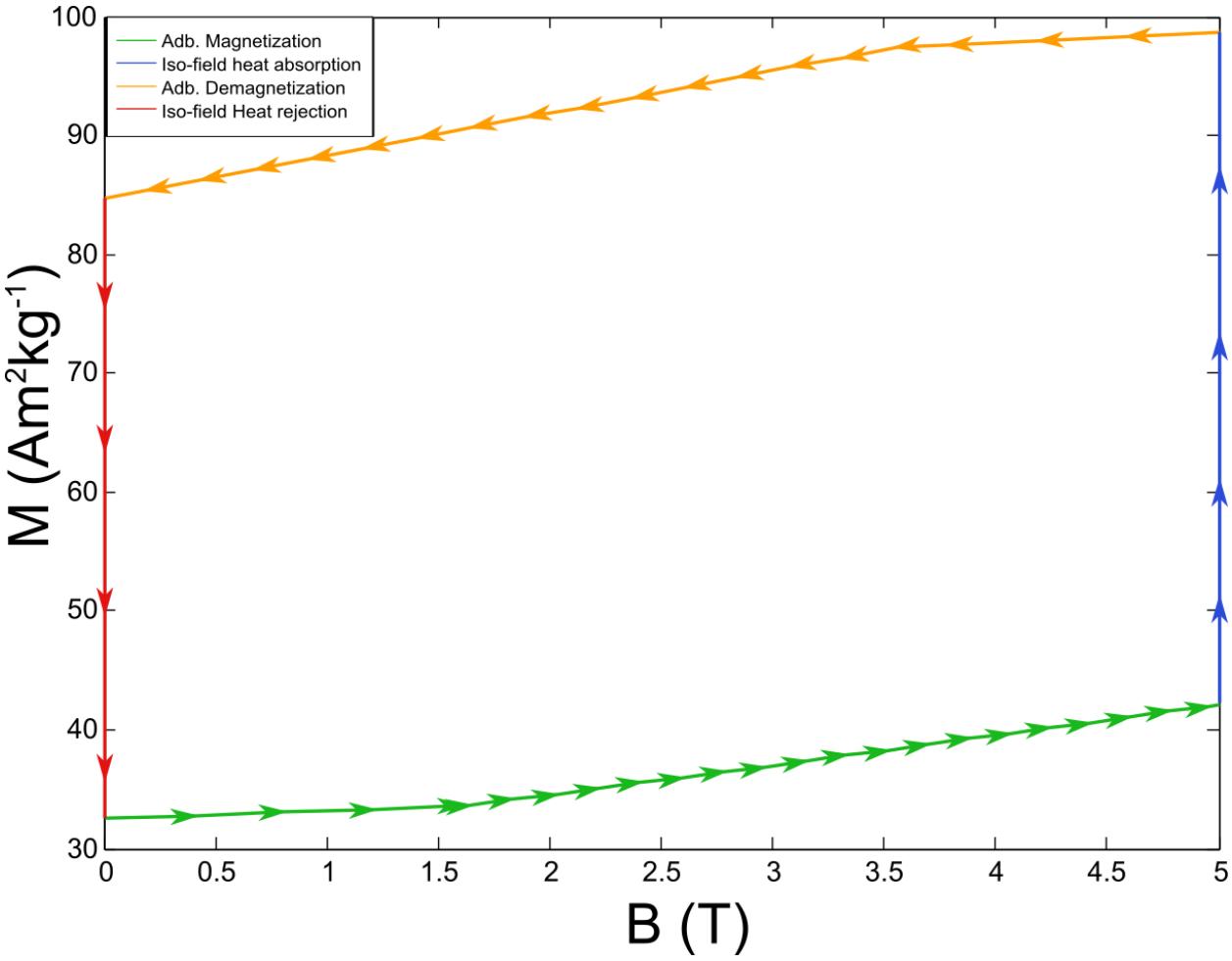

Figure 9: A magnetism vs. field plot for the example Brayton cycle.

Effect of hysteresis on fractional Carnot coefficient of performance

Overview

A useful figure of merit for the thermodynamic performance of a refrigeration cycle is the fractional Carnot coefficient of performance. The coefficient of performance is defined as the

amount of heat removed from the cold reservoir divided by the net work input of the cycle, shown in equation (30).

$$COP_{Brayton} = \frac{Q_{C,removed}}{W_{in}} \tag{30}$$

By the second law of thermodynamics, the highest achievable coefficient of performance is the Carnot coefficient of performance, described in equation (31).

$$COP_{Carnot} = \frac{T_C}{T_H - T_C} \tag{31}$$

T_H and T_C are defined to maximize Q_C and Q_H therefore, they are defined as the temperatures at the end of the cooling and heating legs, respectively. This is shown in Figure 6 and Figure 8. Then, the coefficient of performance of any refrigeration cycle can be compared to the Carnot coefficient of performance by the fractional Carnot coefficient of performance (η), described in equation (32).

$$\eta = \frac{COP_{Brayton}}{COP_{Carnot}} < 1 \tag{32}$$

η was evaluated for Brayton cycles at different hysteresis widths over a range of T_C and T_H values with a magnetic field limit of 1.5 T and 5 T.

COP_{Carnot} of Brayton cycles from 0-1.5 T

Figure 10, Figure 11, and Figure 12, show contour plots of the fractional Carnot coefficient of performance of Brayton cycles operating over magnetic fields between 0 and 1.5 T at ΔT_{Hyst} values of .5, .75, and .1 K, respectively.

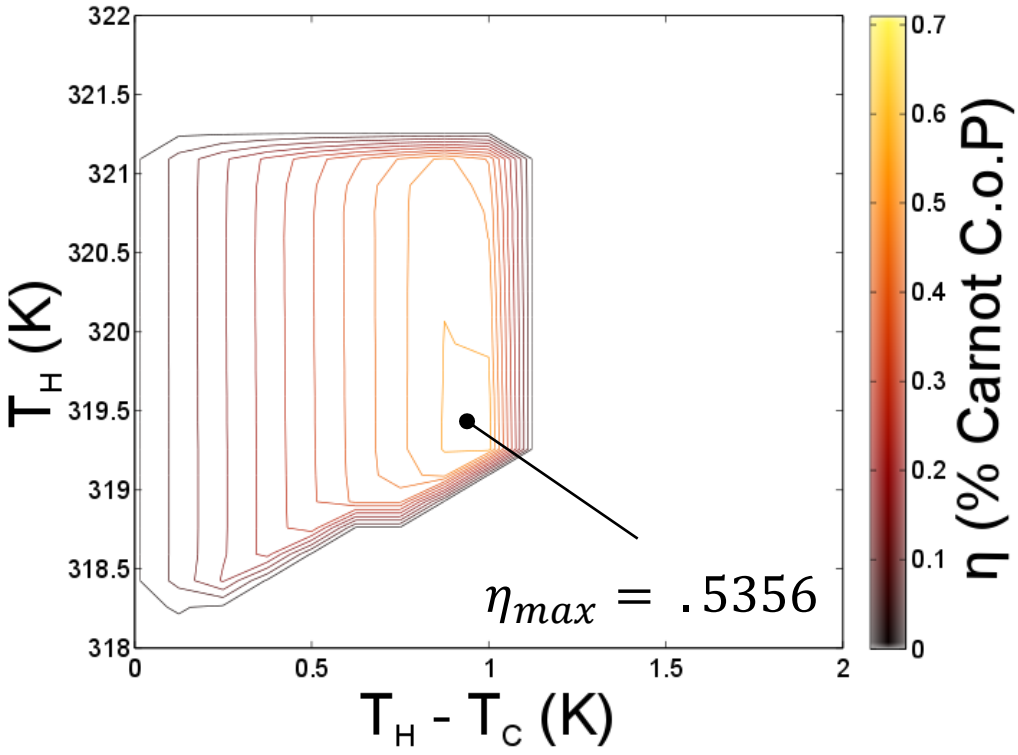

Figure 10: A contour plot of the fractional Carnot efficiency of Brayton cycles simulated from 0-1.5 T at $\Delta T_{Hyst} = .5\ K$.

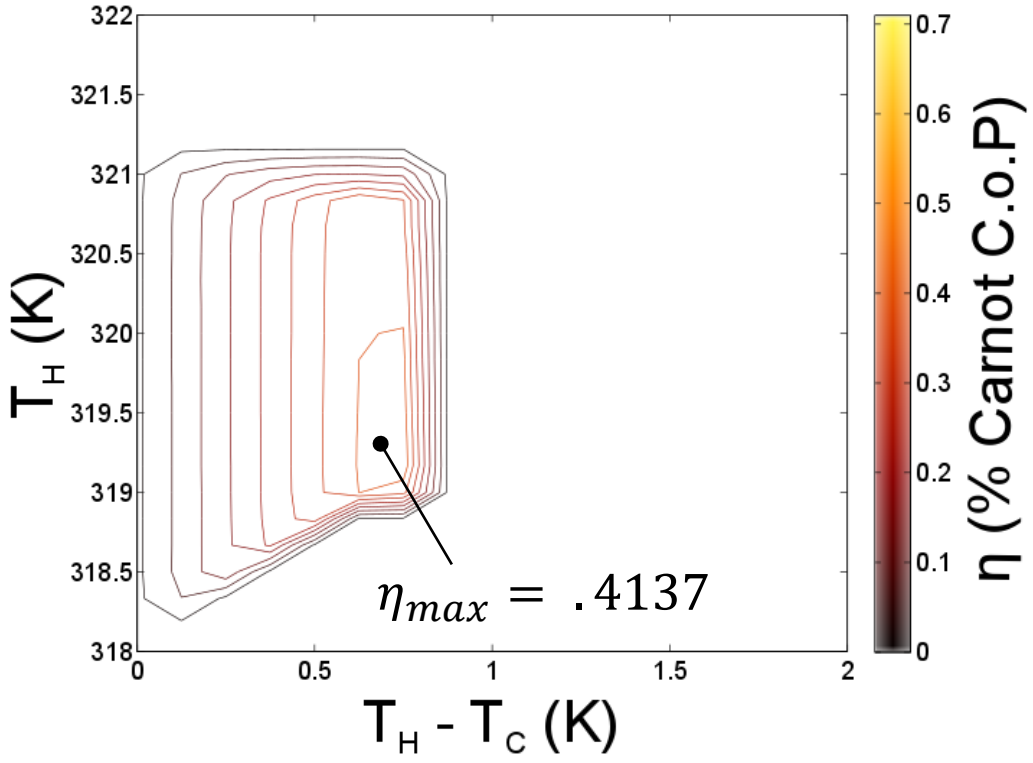

Figure 11: A contour plot of the fractional Carnot efficiency of Brayton cycles simulated from 0-1.5 T at $\Delta T_{Hyst} = .75\ K$.

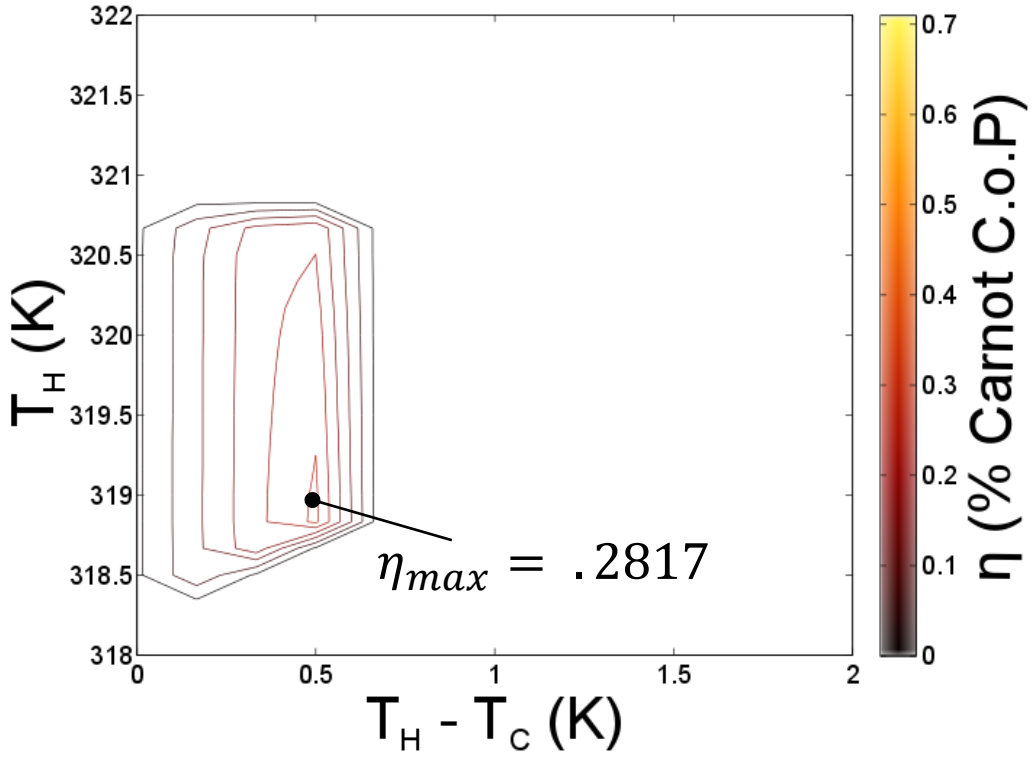

Figure 12: A contour plot of the fractional Carnot efficiency of Brayton cycles simulated from 0-1.5 T at $\Delta T_{Hyst} = 1\ K$.

Fractional Carnot COP of Brayton cycles from 0-5 T

Figure 13, Figure 14, and Figure 15 show contour plots of the fractional Carnot COP over the viable range of T_C and T_H values for cycles from 0-5 T at ΔT_{Hyst} values of 1, 2, and 4 K respectively.

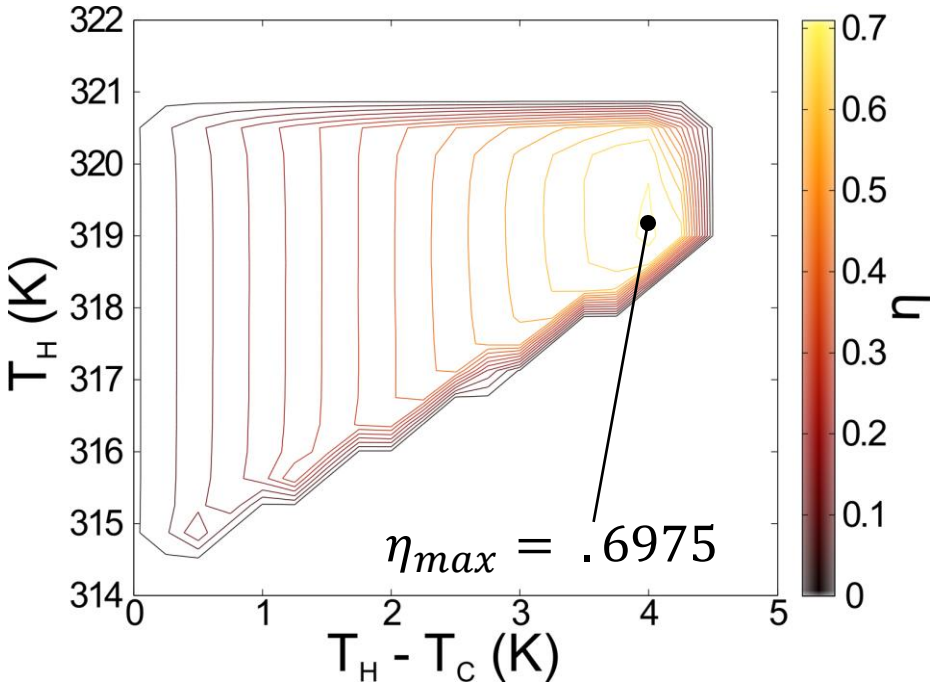

Figure 13: A contour plot of the fractional Carnot efficiency of Brayton cycles simulated from 0-5 T with $\Delta T_{Hyst} = 1\ K$.

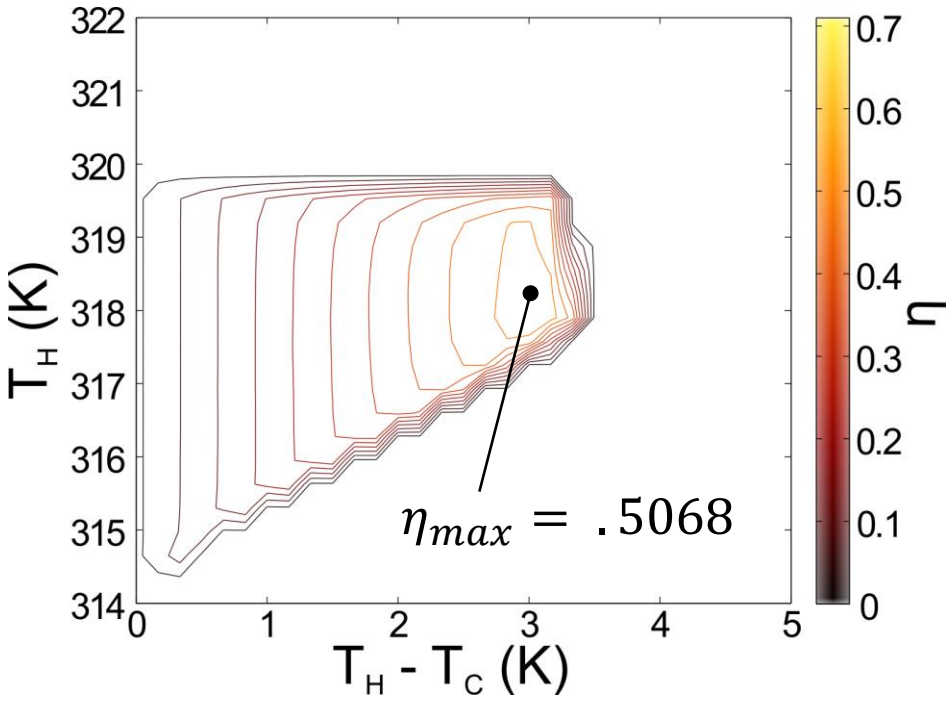

Figure 14: A contour plot of the fractional Carnot efficiency of Brayton cycles simulated from 0-5 T with $\Delta T_{Hyst} = 2K$.

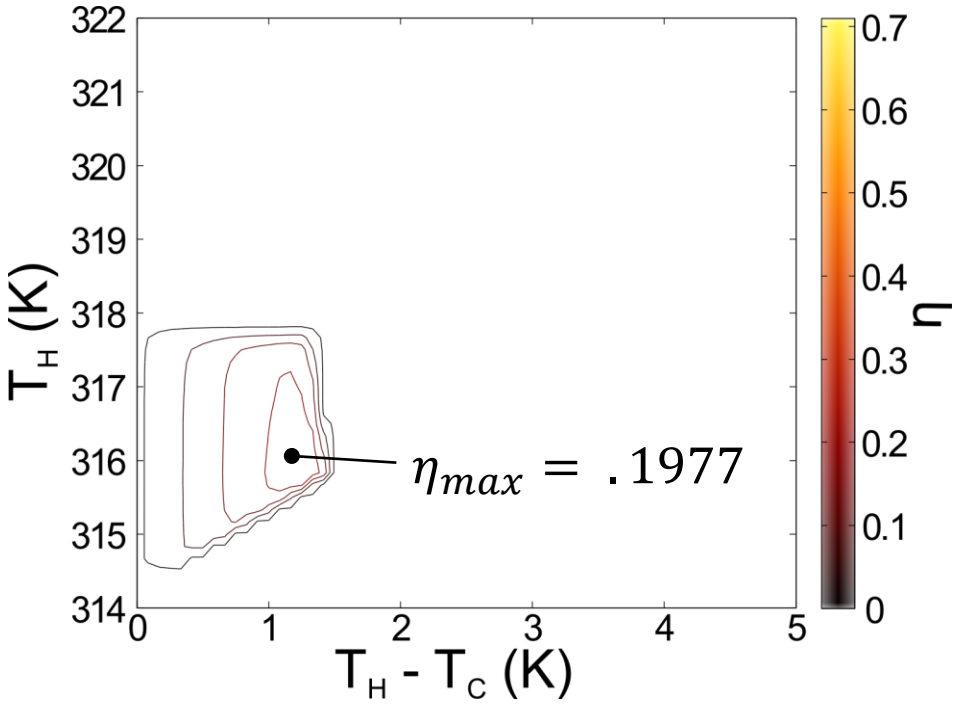

Figure 15: A contour plot of the fractional Carnot efficiency of Brayton cycles simulated from 0-5 T with $\Delta T_{Hyst} = 4\ K$.

Figure 16 shows a plot of the highest observed fractional Carnot COP at each of the hysteresis widths for Brayton cycles ran from 0-5 T.

Summary of results

Figure 16 shows the highest calculated fractional Carnot COP vs. hysteresis width.

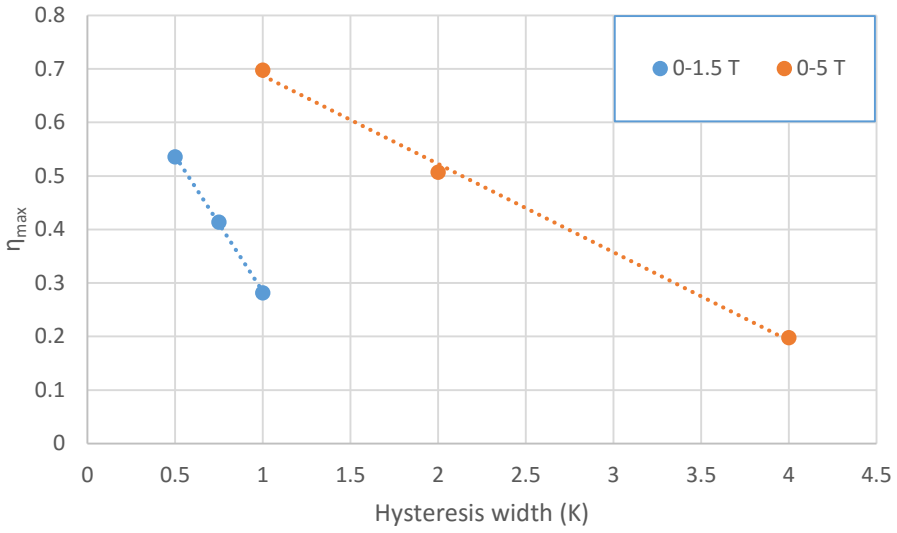

Figure 16: The highest calculated fractional Carnot COP vs. hysteresis width

Brayton cycles that maximize η

Figures 10-15 show that there is a set of T_C and T_H values that optimize η for all hysteresis widths and both field limits. In all cases, this occurs when T_H is equal to $\theta_{f,\beta\to\alpha}$, the temperature at which the $\beta \to \alpha$ transition completes at zero field. An example of one of these "optimal" Brayton cycles is shown in T-B space in Figure 17 and in ϕ-θ space in Figure 18.

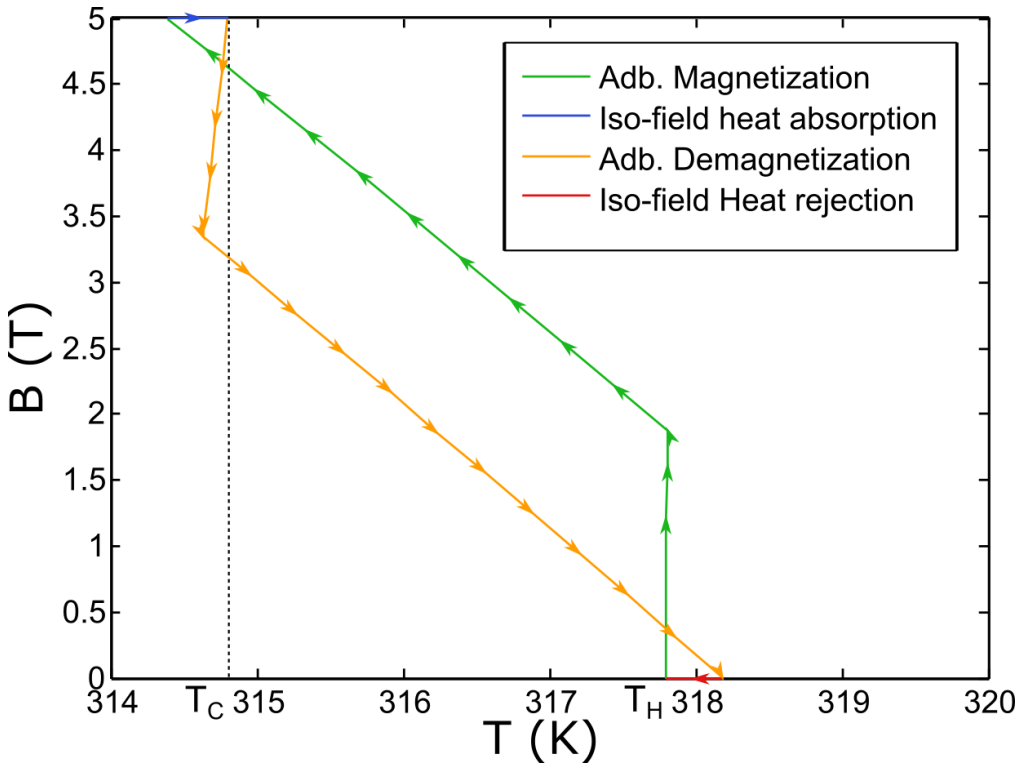

Figure 17: A T-B diagram of the Brayton cycle with the highest fractional Carnot COP at $\Delta T_{Hyst} = 2K$ from 0-5 T.

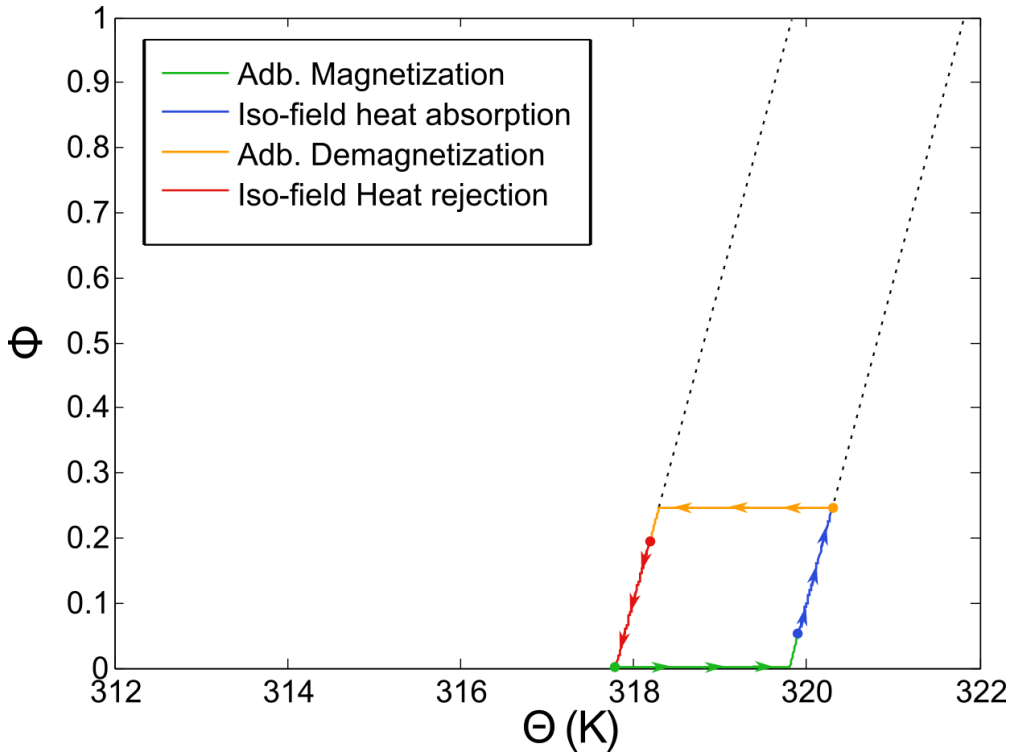

Figure 18: A ϕ vs θ diagram of the Brayton cycle with the highest fractional Carnot COP at $\Delta T_{Hyst} = 2K$ from 0-5 T.

Effect of hysteresis on heat absorbed from a cold reservoir

Overview

Another figure of merit for a cycle's thermodynamic performance is the amount of heat it absorbs from the cold reservoir.

Heat removed of Brayton cycles from 0-1.5 T

Figure 19, Figure 20, and Figure 21 show the amount of heat removed over the viable range of T_H and T_C values for Brayton cycles ran from 0-1.5 T with ΔT_{Hyst} values of .5, .75, and 1 K respectively.

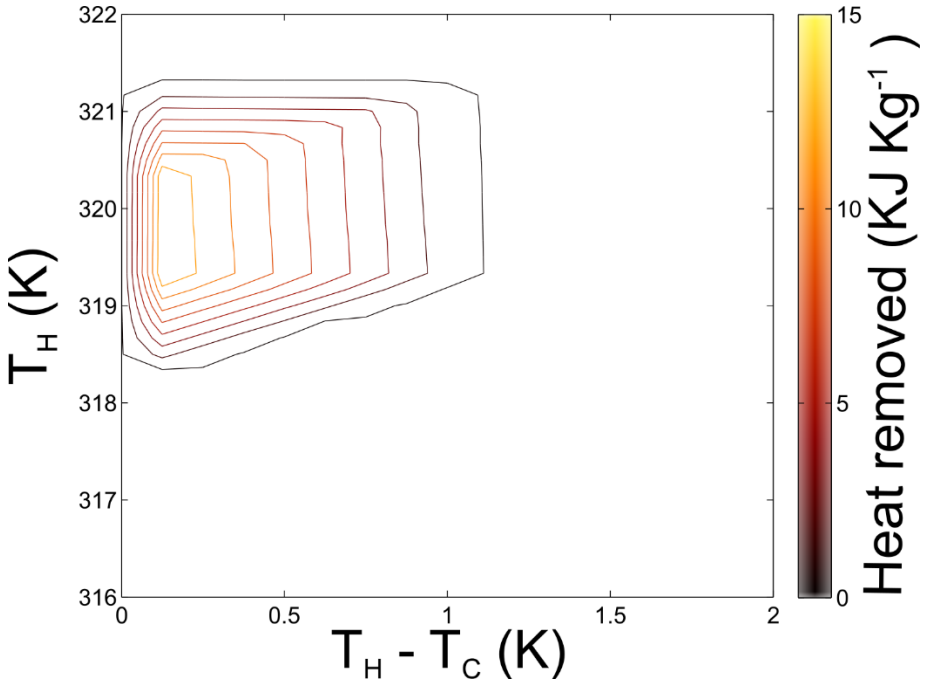

Figure 19: A contour plot of the heat removed from a cold reservoir with Brayton cycles simulated from 0-1.5 T at $\Delta T_{Hyst} = .5$ K.

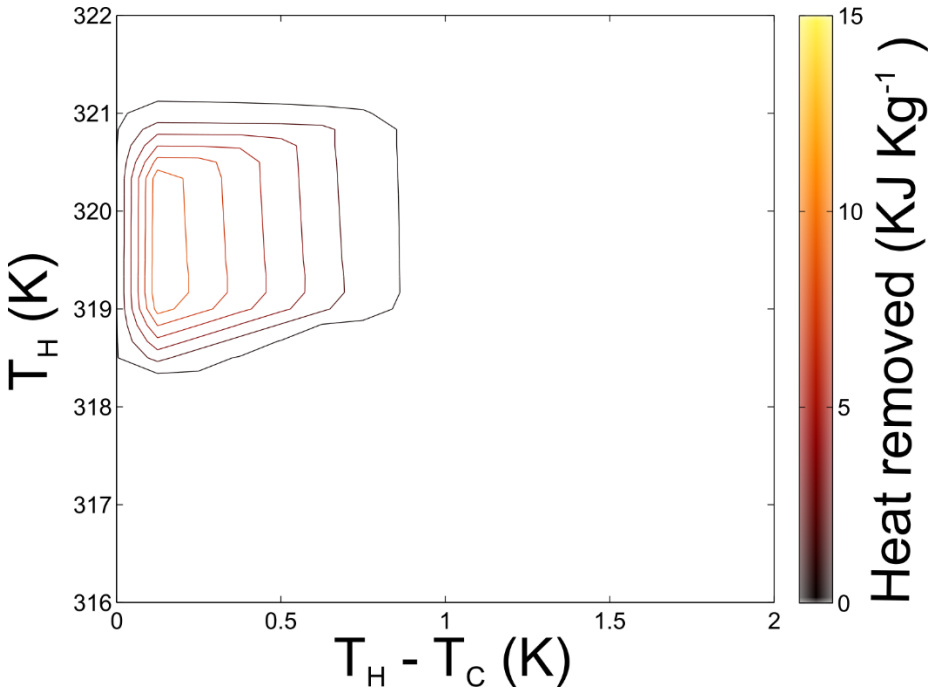

Figure 20: A contour plot of the heat removed from a cold reservoir with Brayton cycles simulated from 0-1.5 T at $\Delta T_{Hyst} = .75\ K$.

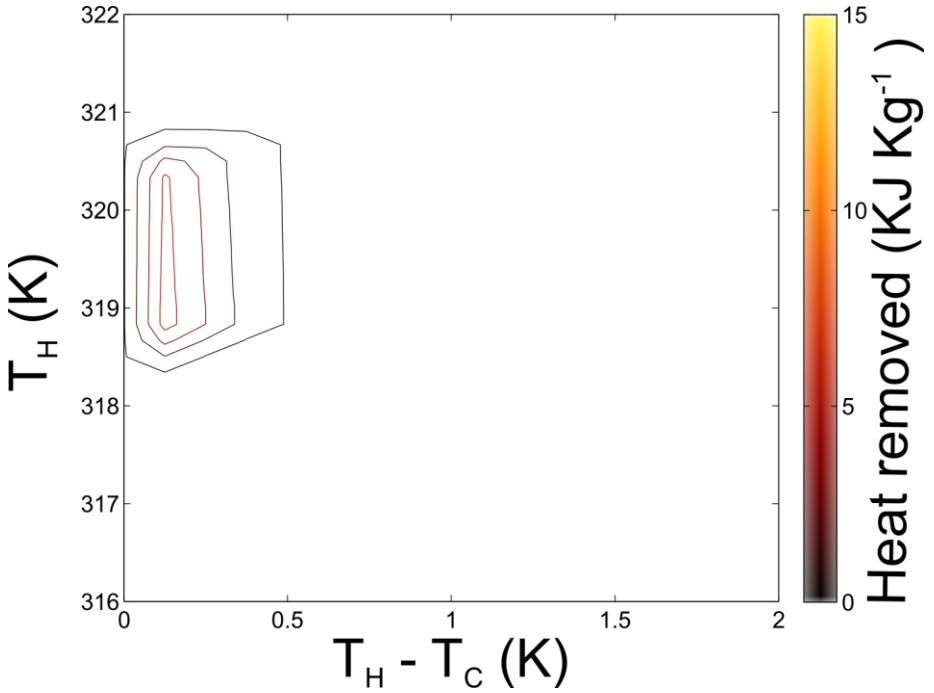

Figure 21: A contour plot of the heat removed from a cold reservoir with Brayton cycles simulated from 0-1.5 T at $\Delta T_{Hyst} = 1\ K$.

Heat removed of Brayton cycles from 0-5 T

Figure 22, Figure 23, and Figure 24 show the amount of heat removed from the cold reservoir for Brayton cycles ran from 0-5 T with ΔT_{Hyst} values of 1, 2, and 4 K respectively.

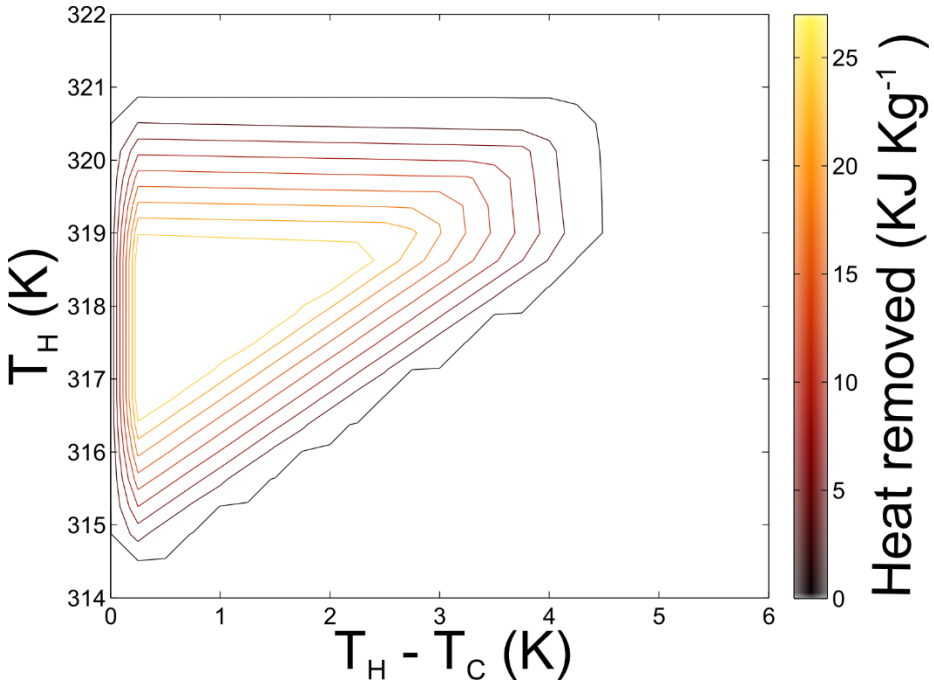

Figure 22: A contour plot of the heat removed from a cold reservoir with Brayton cycles simulated from 0-5 T at $\Delta T_{Hyst} = 1\ K$.

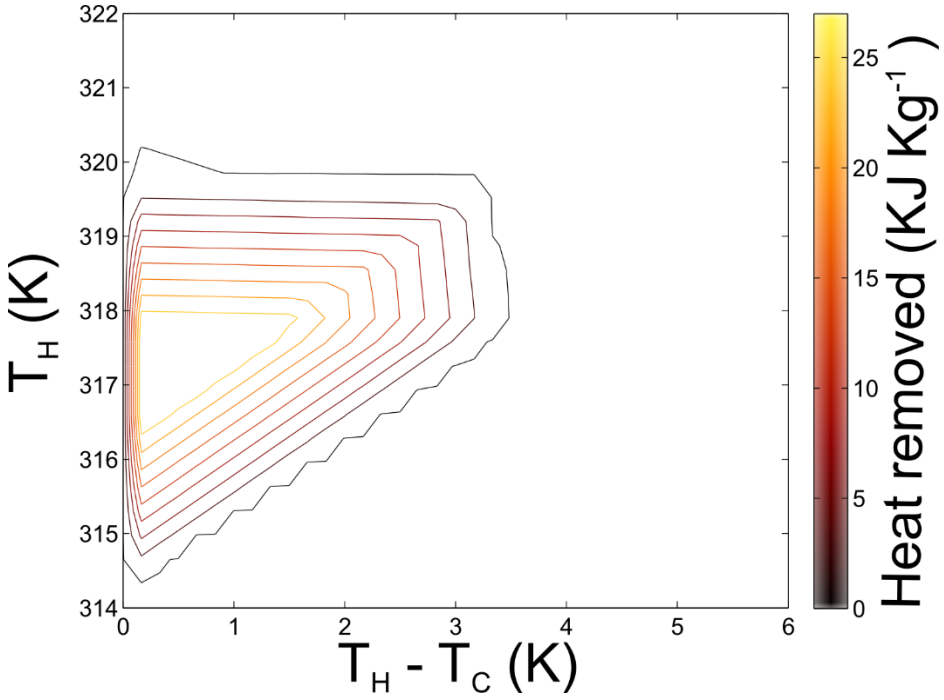

Figure 23: A contour plot of the heat removed from a cold reservoir with Brayton cycles simulated from 0-5 T at $\Delta T_{Hyst} = 2K$.

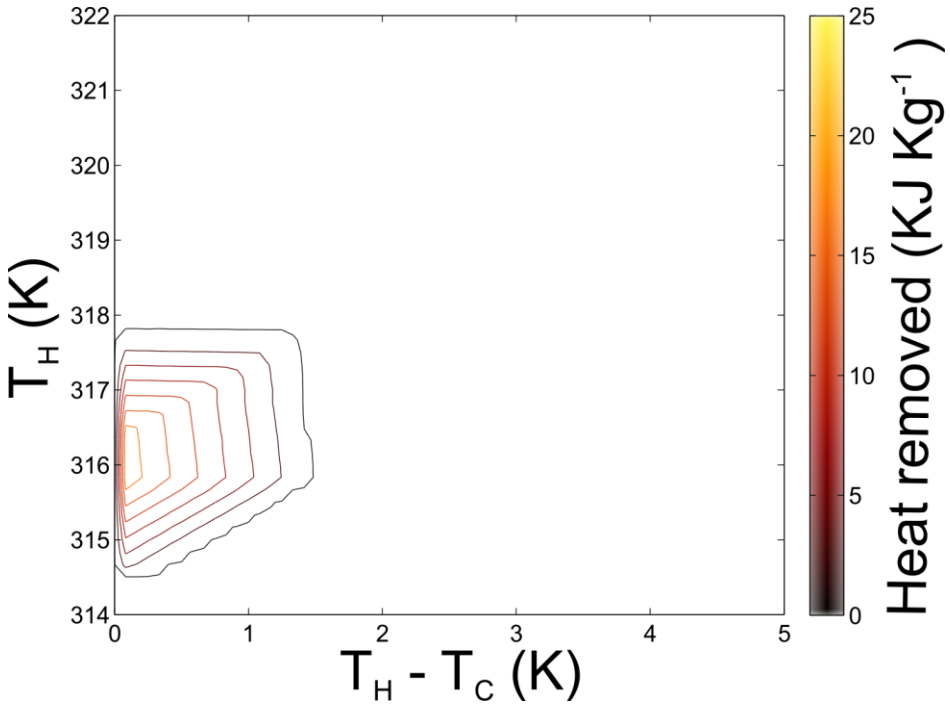

Figure 24: A contour plot of the heat removed from a cold reservoir with Brayton cycles simulated from 0-5 T at $\Delta T_{Hyst} = 4\ K$.

Effect of hysteresis on the net work input of Brayton cycles

Net magnetic work of Brayton cycles from 0-1.5 T

Figure 25, Figure 26, and Figure 27 show the net magnetic work input for Brayton cycles simulated from 0-1.5 T with hysteresis widths of .5, .75, and 1 K respectively.

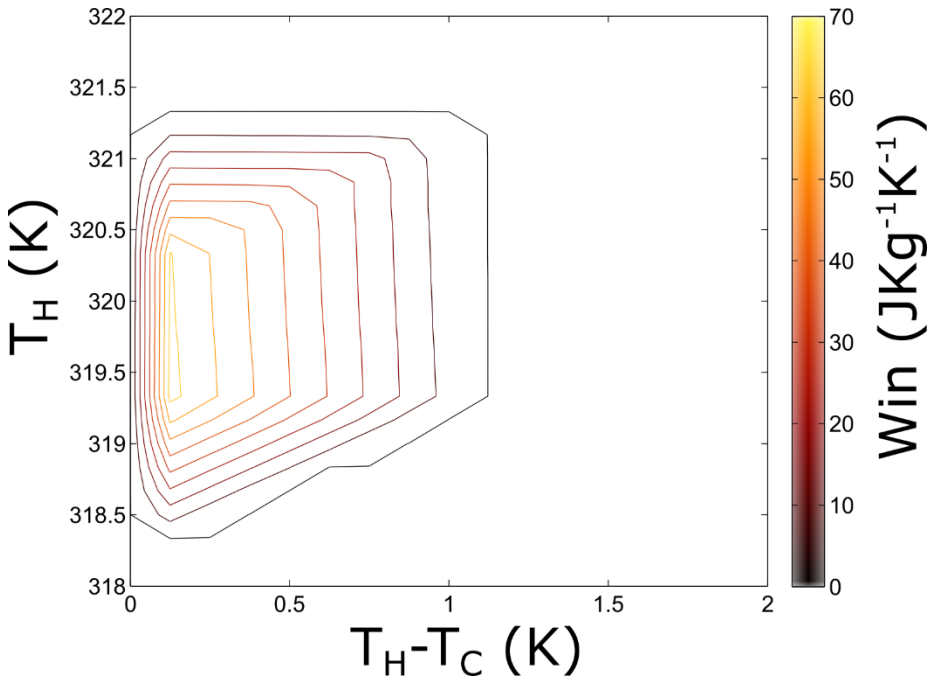

Figure 25: A contour plot of the net work input with Brayton cycles simulated from 0-1.5 T at $\Delta T_{Hyst} = .5\ K$.

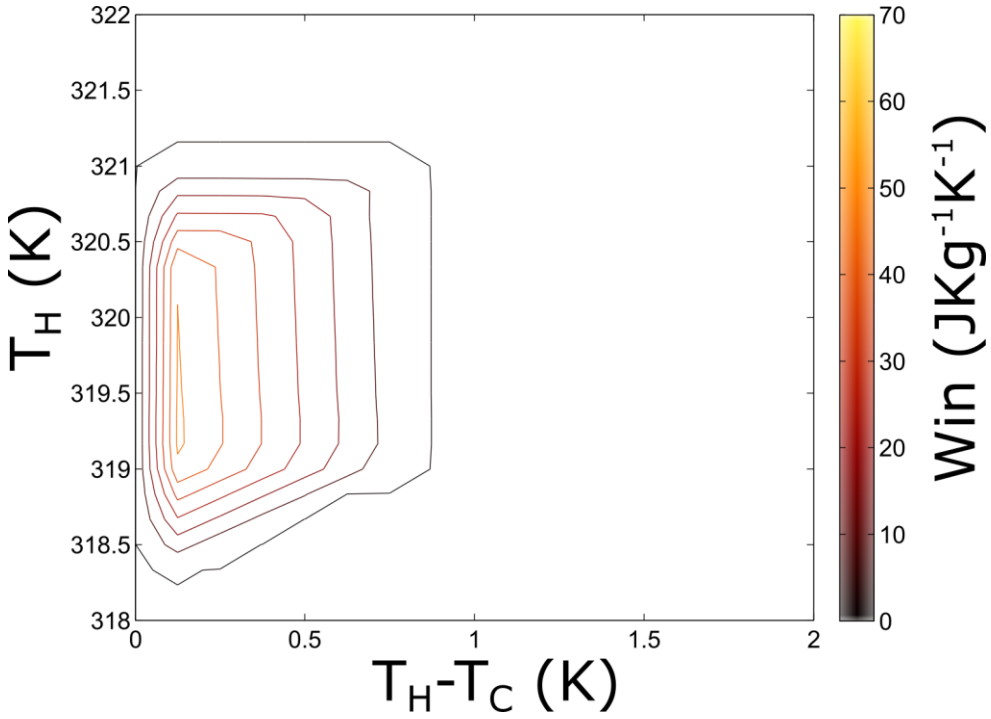

Figure 26: A contour plot of the net work input with Brayton cycles simulated from 0-1.5 T at $\Delta T_{Hyst} = .75\ K$.

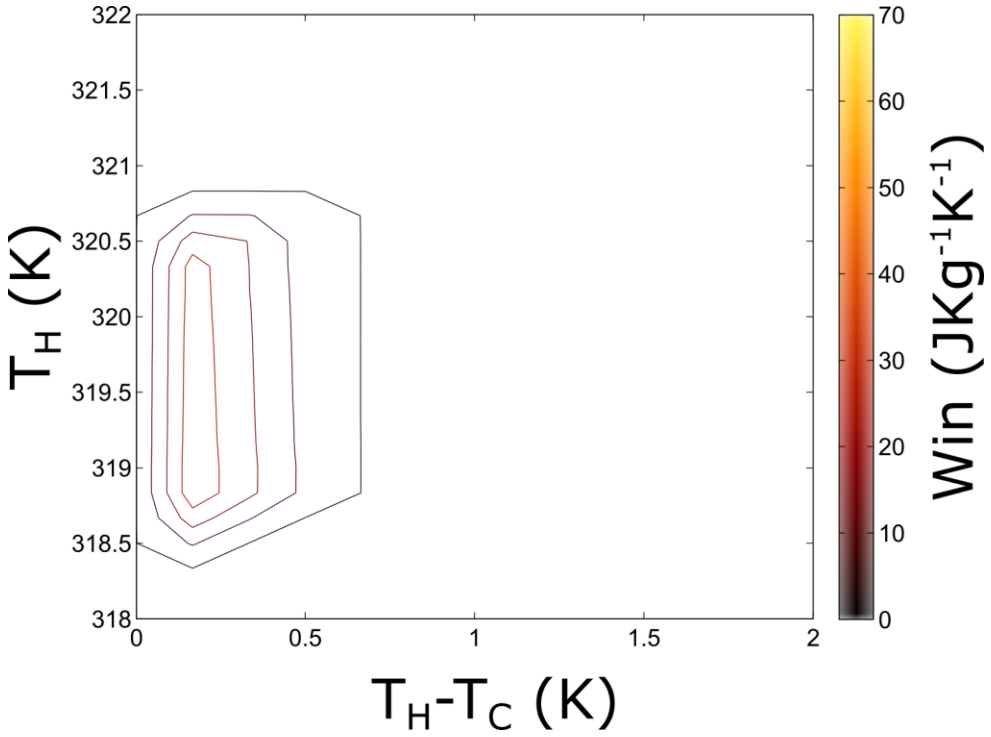

Figure 27: A contour plot of the net work input with Brayton cycles simulated from 0-1.5 T at $\Delta T_{Hyst} = 1\ K$.

Net magnetic work of Brayton cycles from 0-5 T

Figure 28, Figure 29, and Figure 30 show the net magnetic work input for Brayton cycles simulated from 0-5 T with hysteresis widths of 1, 2, and 4 K respectively.

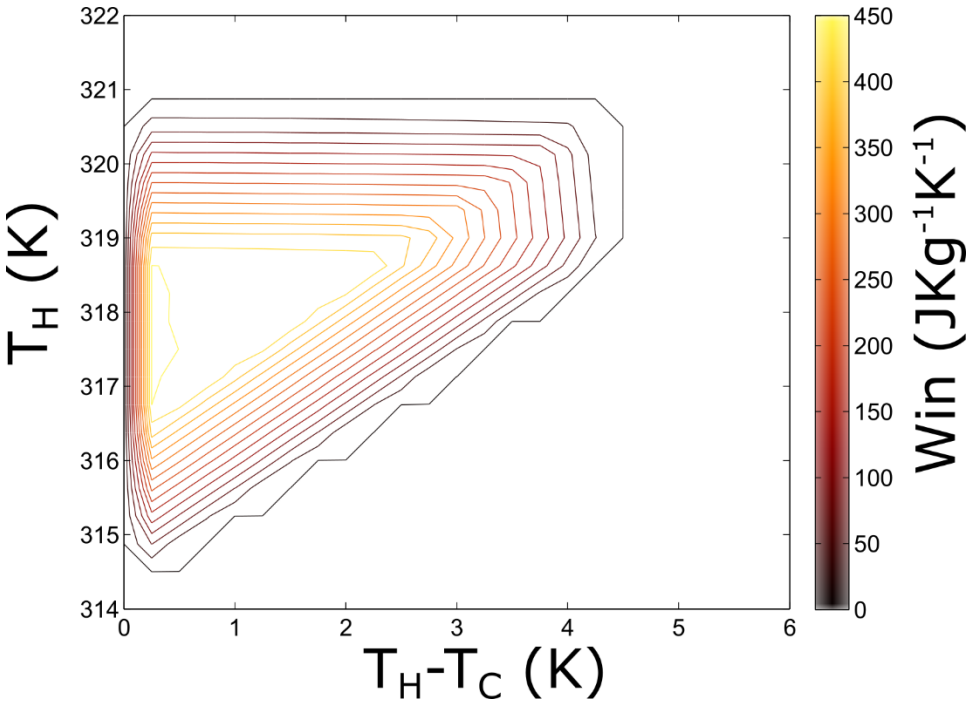

Figure 28: A contour plot of the net work input with Brayton cycles simulated from 0-5 T at $\Delta T_{Hyst} = 1\ K$.

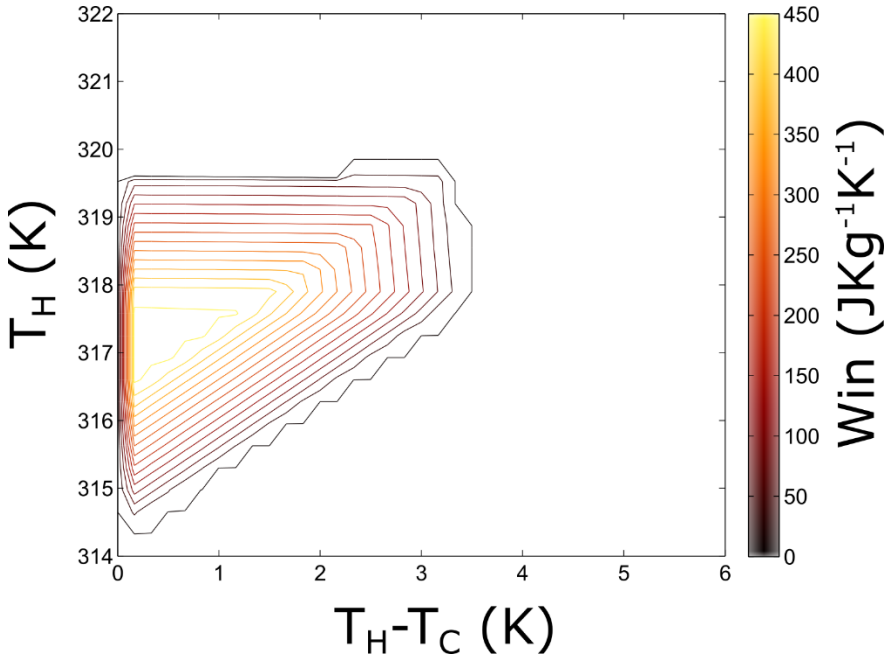

Figure 29: A contour plot of the net work input with Brayton cycles simulated from 0-5 T at $\Delta T_{Hyst} = 2\ K$.

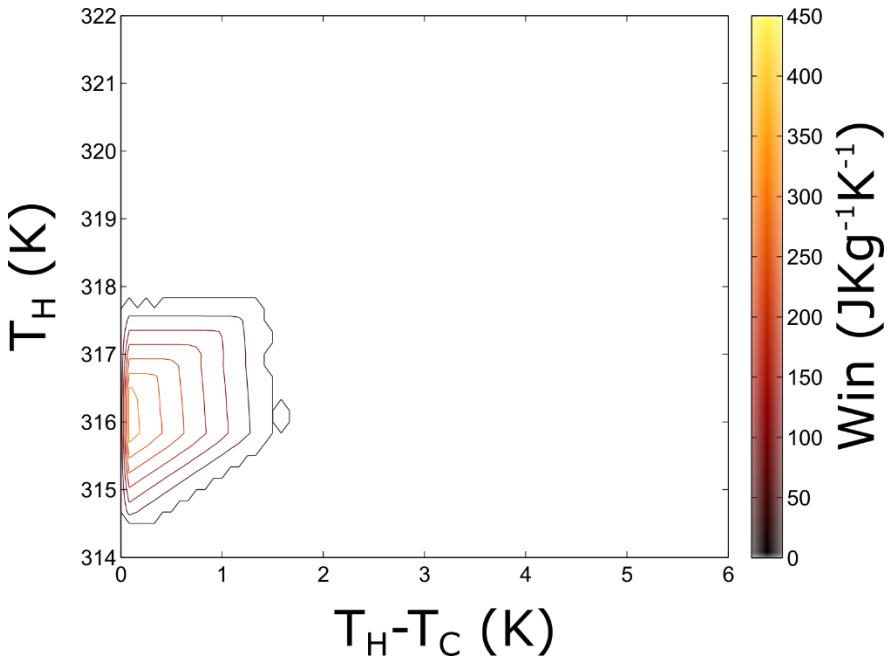

Figure 30: A contour plot of the net work input with Brayton cycles simulated from 0-5 T at $\Delta T_{Hyst} = 4\ K$.

CHAPTER IV

CONCLUSIONS AND FUTURE WORK

Conclusions

As shown in Figures 10-15, increasing the hysteresis width has several consequences on the thermodynamic performance of Brayton cycles ran from both 0-1.5 T and 0-5 T. Increasing the hysteresis width reduces the highest fractional Carnot COP that can be achieved ($\eta_{\max}$). Furthermore, it also reduces the range of T_C and T_H values for which viable Brayton cycles are possible, represented by the decreasing size of the contour plots in Figures 10-15.

The results indicate that there is a linear decrease in the maximum observed fractional Carnot COP with increasing ΔT_{Hyst}. Extrapolating from the regression lines in Figure 16, it appears that successful Brayton cycles are not possible when the hysteresis width exceeds 1.6 K for cycles limited to 1.5 T fields or when the hysteresis width exceeds 5.2 K for cycles limited to 5 T fields. Figure 16 can also be used to estimate the hysteresis width limit for a desired fractional Carnot COP. For example, if a designer requires 50 % of Carnot COP for a refrigerator with a field limit of 1.5 T, the hysteresis width should not exceed 2 K. It should also be noted that the regression lines do not predict a 100% Carnot COP when there is no hysteresis. This is because T_C and T_H have been selected to maximize heat absorption and rejection, rather than the COP.

Figures 19-24 show that an increasing hysteresis width also reduces the amount of heat that can be removed from a cold reservoir for Brayton cycles simulated from 0-1.5 T and 0-5 T. Also, for a given hysteresis width, the T_H that maximizes the heat removed from the cold reservoir is the

same T_H that maximizes the fractional Carnot COP. However, the T_C that maximizes the heat removed from the cold reservoir is different from the T_C that maximizes the fractional Carnot COP. This is shown with a comparison of Figures 10-15 and 19-24. This is because the fractional Carnot coefficient of performance takes into account the temperature span ($T_H - T_C$). Although raising T_C allows the material to absorb more heat from the cold reservoir before reaching T_C it also raises the possible COP (equation (31)). This in turn reduces the fractional Carnot COP. Furthermore, a comparison of Figures 19-24 and 25-30 shows that the work input is maximized when the heat removed from the cold reservoir is maximized. This offers another reason why maximizing the heat removed from the cold reservoir does not necessarily maximize the fractional Carnot COP.

Based on these results, it is recommended that GMCE based Brayton cycles be ran at $T_H = \theta_{f,\beta\to\alpha}$, but the choice of T_C is dependent on the relative importance of a large temperature span over a large quantity of heat removed per cycle.

Future Work

Our research team has already developed models for Ericsson cycles [7], so there is room to compare the computational results of Ericsson and Brayton cycles. Furthermore, we plan to add regenerative legs to the existing Brayton cycle methodology. This would include changing how T_H and T_C are defined. There are also other cycles that we would like to consider, including one that involves constant driving force legs. Lastly, we would like to apply this modeling methodology to other materials, including "direct" GMCE materials, which exhibit adiabatic

temperature increases or isothermal entropy reductions when placed in a magnetic field that induces an $\alpha \rightarrow \beta$ transition.

REFERENCES

1. Coulumb, D. *The IIR and the Environmental Challenges Facing the Refrigeration Sector*. in *Proceedings of IIR International Conference on Magnetic Refrigeration at Room Temperature*. 2007.

2. Russek, S.L. and C.B. Zimm, *Potential for cost effective magnetocaloric air conditioning systems.* International Journal of Refrigeration, 2006. **29**(8): p. 1366-1373.

3. Gschneidner, K. and V. Pecharsky, *Thirty years of near room temperature magnetic cooling: Where we are today and future prospects.* International journal of refrigeration, 2008. **31**(6): p. 945-961.

4. Gschneidner, K., *The magnetocaloric effect, magnetic refrigeration and ductile intermetallic compounds.* Acta Materialia, 2009. **57**(1): p. 18-28.

5. Pecharsky, V.K. and K.A. Gschneidner Jr, *Magnetocaloric effect and magnetic refrigeration.* Journal of Magnetism and Magnetic Materials, 1999. **200**(1): p. 44-56.

6. Engelbrecht, K.L., G.F. Nellis, and S.A. Klein, *Predicting the performance of an active magnetic regenerator refrigerator used for space cooling and refrigeration.* HVAC&R Research, 2006. **12**(4): p. 1077-1095.

7. Brown, T.D., et al., *A Preisach-Based Nonequilibrium Methodology for Simulating Performance of Hysteretic Magnetic Refrigeration Cycles.* JOM, 2015. **67**(9): p. 2123-2132.

8. Brown, G., *Magnetic heat pumping near room temperature.* Journal of Applied Physics, 1976. **47**(8): p. 3673-3680.

9. Pecharsky, V.K. and K.A. Gschneidner Jr, *Giant magnetocaloric effect in Gd 5 (Si 2 Ge 2).* Physical review letters, 1997. **78**(23): p. 4494.

10. Wada, H., et al., *Giant magnetocaloric effect of MnAs 1− x Sb x in the vicinity of first-order magnetic transition.* Physica B: Condensed Matter, 2003. **328**(1): p. 114-116.

11. Pecharsky, V. and K. Gschneidner Jr, *The giant magnetocaloric effect in Gd5 (SixGe1-x) 4 materials for magnetic refrigeration*, in *Advances in cryogenic engineering*. 1998, Springer. p. 1729-1736.

12. Sharma, V., M. Chattopadhyay, and S. Roy, *Large inverse magnetocaloric effect in Ni50Mn34In16.* Journal of Physics D: Applied Physics, 2007. **40**(7): p. 1869.

13. Wada, H. and Y. Tanabe, *Giant magnetocaloric effect of MnAs1− xSbx.* Applied Physics Letters, 2001. **79**(20): p. 3302-3304.

14. Zhang, H., et al., *Reduction of hysteresis loss and large magnetocaloric effect in the C- and H-doped La (Fe, Si) 13 compounds around room temperature.* Journal of Applied Physics, 2012. **111**(7): p. 07A909.

15. Cross, C., et al., *Optimal temperature-entropy curves for magnetic refrigeration*, in *Advances in cryogenic engineering*. 1988, Springer. p. 767-775.

16. Steyert, W., *Stirling-cycle rotating magnetic refrigerators and heat engines for use near room temperature.* Journal of Applied Physics, 1978. **49**(3): p. 1216-1226.

17. Barclay, J., *Use of a ferrofluid as the heat-exchange fluid in a magnetic refrigerator*. Journal of Applied Physics, 1982. **53**(4): p. 2887-2894.

18. Mayergoyz, I.D., *Mathematical models of hysteresis and their applications*. 2003: Academic Press.

19. Mayergoyz, I.D., *Mathematical models of hysteresis.* Magnetics, IEEE Transactions on, 1986. **22**(5): p. 603-608.

20. Kihara, T., et al., *Direct measurements of inverse magnetocaloric effects in metamagnetic shape-memory alloy NiCoMnIn.* Physical Review B, 2014. **90**(21): p. 214409.

21. Shamberger, P.J. and F. Ohuchi, *Hysteresis of the martensitic phase transition in magnetocaloric-effect Ni-Mn-Sn alloys.* Physical Review B, 2009. **79**(14): p. 144407.

22. Çengel, Y.A., et al., *Fundamentals of thermal-fluid sciences*. 2008: McGraw-Hill New York.

23. T.D. Brown, P.J.S., *Improving GMCE-Based Refrigeration: Modeling Magnetic Entropy Change Effects in Hysteretic Systems*. 2015, Texas A&M University.